Interfacial fatigue debonding retardation in wrapped composite joints
Experimental and numerical study

Feng, Weikang; Pavlovic, Marko; Koetsier, Mathieu; Veljkovic, Milan

DOI
10.1016/j.compstruct.2023.117146

Publication date
2023

Document Version
Final published version

Published in
Composite Structures

Composite Structures 319 (2023) 117146

Contents lists available at ScienceDirect

Composite Structures

journal homepage: www.elsevier.com/locate/compstruct

Interfacial fatigue debonding retardation in wrapped composite joints: Experimental and numerical study

Weikang Feng, Marko Pavlovic *, Mathieu Koetsier, Milan Veljkovic

Faculty of Civil Engineering and Geoscience, Delft University of Technology, 2600AA, Delft, the Netherlands

ARTICLE INFO

Keywords:
Fatigue crack propagation
Friction effect
3D DIC
Optical fiber
Finite element modelling
VCCT

ABSTRACT

Debonding crack propagation at the composite-to-steel interface has been found to be an important failure mechanism for wrapped composite joints under static and fatigue loads. Friction at the interface behind the crack tip may deviate fatigue debonding of the joints from the linear-fracture-mechanics behaviour. This paper presents static and fatigue tests of axial wrapped composite joints. 3D DIC and optical fiber system is employed to monitor displacements and crack propagation. A finite element model is established and validated against static and fatigue test results, where friction is considered at the cracked interface. Through FE modelling, it is proved that the friction at the interface significantly reduce the strain energy release rate (SERR) at the crack tip, leading to retardations of crack growth and stiffness degradation. Parametric study is conducted finally to investigate the influence of friction coefficient, failure modes as well as Paris relationship parameters on the predicted fatigue behaviour of wrapped composite joints.

1. Introduction

Wrapped composite joint, an innovative joining technique recently developed at TUD, has been proposed to improve the fatigue performance of joints for steel hollow sections [1,2]. Instead of connecting steel tubes by welding or by using casted joints, the wrapped composite joints utilize bonded composite wrap to transfer forces between steel members. Their fatigue lifetime was experimentally shown to be 10–100 times longer than their welded counterparts under the same load level [3]. Under fatigue loading, the stiffness of wrapped composite joints degrades steadily due to the debonding at the composite-to-steel interface, which is mainly mode II debonding crack development [3,4]. During recent studies on uniaxial joints, as shown in Fig. 1 (a), the stiffness degradation rate of the joints shows a decreasing trend under cyclic loads. Correspondingly, the crack propagation monitored by DIC shows a retardation phenomenon, as schematically shown by solid lines in Fig. 1 (b). Whereas the FEA shows that the SERR values along the debonding path should remain constant within the region of uniform wrap thickness (see Fig. 1 (c), where a_c is length of the region of uniform wrap thickness). Subsequently, a crack growth with no retardation and stiffness degradation without any retardation should be achieved (see dashed lines in Fig. 1 (b)). This paper aims to simulate and explain this contradictory phenomenon to provide better prediction tools and design recommendations for the wrapped composite joint.

One possible reason for crack growth retardation in bonded interfaces is fiber bridging, which has been widely investigated in the literature [5]. The fibers of adjacent plies bridges the delamination plane and act as crack arrestors, due to which the delamination resistance and interlaminar fracture toughness increases. Hwuang et al. [6] and Yao et al. [7] reported that the fatigue crack growth of composite laminates under mode I cyclic loading experienced a significant retardation phenomenon at a given strain energy release rate due to the presence of fiber bridging. The fatigue resistance curve moves from the left to the right, namely, the Paris relationship parameter C decreases as fiber bridging develops [8]. Holmes et al. [9] also found that as the bridging zone develops, the crack growth rate decreases until the bridging zone is fully developed. After that a steady-state crack growth can be achieved. In order to remove the fiber bridging dependency of Paris relationship, Shivakumar et al. [10], Chen et al. [11] and Liu et al. [12] normalized G against the fracture toughness $G_c(a)$. Paris curves of different extents of fiber bridging collapsed into one single master curve by this kind of normalization. Yao et al. [7] argued that the magnitude of fiber bridging during the fatigue loading is different from that during the quasi-static loading. It is incorrect to apply the R-curve from quasi-static test to normalize the Paris equation. Yao et al. [7] found that bridging caused by fatigue delamination is less obvious than in quasi-static delamination

* Corresponding author.
E-mail address: M.Pavlovic@tudelft.nl (M. Pavlovic).

https://doi.org/10.1016/j.compstruct.2023.117146
Received 9 January 2023; Received in revised form 25 April 2023; Accepted 10 May 2023
Available online 15 May 2023

for multi-directional laminates. They proposed another way to exclude the influence of fiber bridging when establishing the Paris relation [13]. In their study, the strain energy release rates were decomposed into two mechanisms, namely $G = G_{br} + G_{tip}$, where G_{br} represents SERR in fiber bridging and G_{tip} represents the SERR around crack tip. The fatigue growth driving force is chosen as an effective SERR range ΔG_{eff}, which is only expressed as a function of G_{tip}. However, Keisuke et al. and James et al. [14,15] investigated the fiber bridging effect for different mixed-modes. It was found that fiber bridging effect in mode II fatigue cracks is not as pronounced as that in mode I case. Keisuke et al. [14] found that the propagation rate of mode II interlaminar fatigue cracks is nearly constant when the SIF range is kept constant, indicating that the fiber bridging is minimal for mode II cracks. James et al. [15] investigated the influence of mixed mode I and mode II loading on fatigue delamination growth characteristics of composite laminates. It was also shown that bridging fibers yielded a reduced influence over growth rate under increasing mode-II loading conditions. It can be seen from the discussion above that most research related to the fiber bridging effect is mainly limited to mode I fatigue delamination within composite laminates. It is still not proved whether fiber bridging effect is pronounced or not for mode II fatigue debonding at the composite-to-metal interface.

Another reason which may lead to the decreased crack growth rate in mode II crack propagation is the friction effect. Friction between cracked surfaces opposes its sliding direction under mode II crack propagation and may be a source of an extra energy absorption mechanism, leading to decreased SERR values at the crack tip [16]. Mall et al. [17] investigated the friction effect on fatigue debond growth in adhesively bonded composites under mode II fatigue loading conditions through the ENF test. It was found that the friction at the debonded interface may lead to lower SERR at the crack tip, especially for shorter crack lengths. Higher friction coefficient corresponded to a higher SERR decrease. Carlsson et al. and Gillespie et al. [18] also studied the friction effect in ENF test through finite element modelling. They pointed out that the contact pressure at the interface is mainly distributed over a limited area near the support pin, which may lead to friction force and decrease of SERR of 2–4%. Chengye et al. [19] derived a governing parameter f to quantify the frictional force effect on the G_c value for mode II delamination in ENF and 4ENF specimens. It was found that due to the existence of the friction effect, SERR values of ENF and 4ENF specimens decreased by 2–12% compared to specimens without friction effect considered, and 4ENF test has more significant frictional force effect. Parrinello et al. [20] used a specific cohesive frictional constitutive model to simulate the interfacial behaviour of ENF specimens before and after damage. The results showed that the interlaminar frictional effects produced a considerable energy dissipation contribution during cyclic loading. It can be seen from literature above [16–20] that friction effect has been extensively investigated for beam-type specimens with mode II fracture behaviour, which indeed plays an important role on the SERR values at the crack tip. The friction forces are especially pronounced where there is significant contact pressure at the interface.

Considering the facts that 1) the laminate wrapped around the steel tube may cause contact pressure at the composite-to-steel interface of wrapped composite joints due to contraction of the composite wrap when loaded in tension as well as the pre-strain of the laminates during and after production; 2) the contact area with friction forces between steel and composites is much larger than that in beam-type specimens, it is reasonable to make the assumption that the friction effect at the interface may dissipate part of the input energy, which may serve as the main reason for the crack growth retardation phenomenon observed during the tests presented in this paper.

Except for the two main reasons mentioned above, some other residual interaction at the interface originating from debris built-up, micro wedging, et al. may also contribute to debonding retardation phenomenon observed in the tests. However, these mechanisms can be jointly considered as part of friction effect at the interface. In this paper, the influence of friction effect at the composite-to-steel interface of wrapped composite joint on its debonding behaviour is investigated experimentally and numerically. Static tests on uniaxial wrapped composite joints are conducted to provide reference for the fatigue tests and serve as validation for FE model. Specimens are analysed in terms of stiffness, resistance, and ductility. In the follow-up fatigue tests, the stiffness degradation and crack propagation are monitored by 3D DIC and optical fiber systems. 3D finite element model is established and validated against test results in terms of load–displacement curves and strain distribution on the surface of composite wrap. Virtual Crack Closure Technique (VCCT) in FE, combined with friction behaviour, is defined at the interface, which is used to calculate SERR and to explain the crack growth retardation phenomenon. Crack propagation and stiffness degradation of the joints is predicted based on the SERR values from FE model and the preliminary established Paris relationship. Finally,

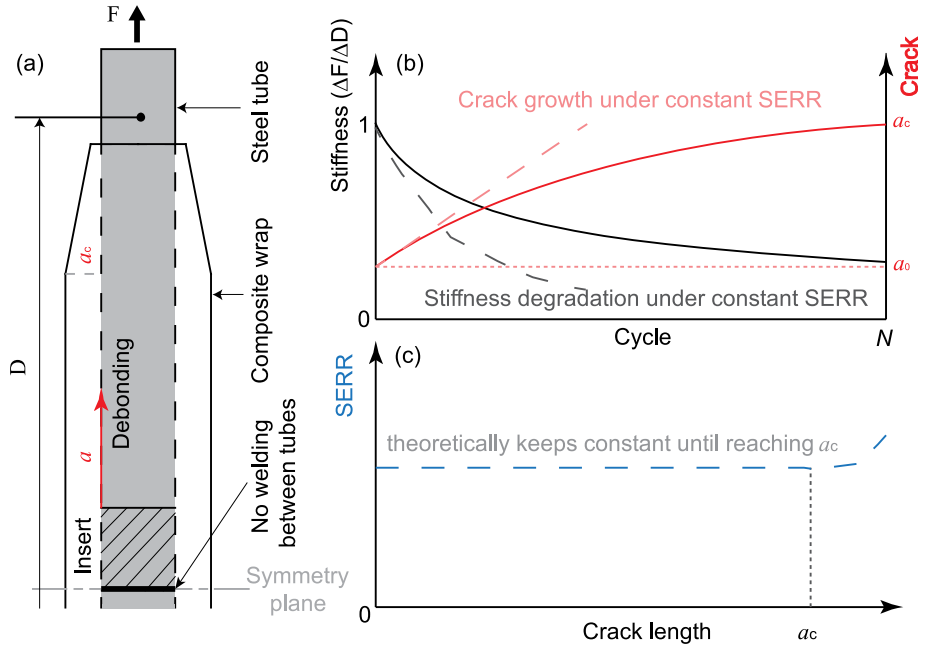

Fig. 1. Schematic of stiffness degradation stabilization and crack growth retardation at the bonded interface of wrapped composite joints.

parametric studies about the influence of friction coefficient, failure modes and Paris relationship parameters on the predicted results are conducted.

2. Experimental study

2.1. Specimens, test set-up and instrumentation

In this study, the A-joint, namely the uniaxial splice joint, is used due to its geometrical simplicity thus the opportunity for clear interpretation of mechanical behaviour of debonding in a simple tensile load condition. In such case, where the wrapping thickness is uniform, the SERR at the crack tip is supposed to be constant as the crack propagates, providing the stable crack propagation in static and constant crack propagation rate under constant amplitude fatigue loading. Geometry and dimensions of specimens are shown in Fig. 2 and all the specimens are summarized in Table 1. Two steel tubes of Φ60.3 × 4 with steel grade S355 are bonded together by composite wrap. Before applying the composites, surfaces of steel tubes were grit blasted and chemically degreased to ensure good bonding between composite laminates and steel tubes. No separate adhesive layer is applied between the composite layer and steel tubes. The laminate of the composite wrap is directly laminated on the steel members and is formed with multi-directional composition of E-glass reinforcement and a vinyl ester resin system. The composite wrapping thickness is 12 mm. The wrapping length for static specimens is 300 mm as shown in Fig. 2 (a), while a longer wrapping with the length of 480 mm as shown in Fig. 2 (b) is used for the fatigue ones in order to have longer stable crack propagation regions. A 25 mm PTFE insert is applied at butt end of each tube forming two separate initial crack tips, such that the uncertainties related to crack initiation are reduced. A matt white paint is applied on the wrap, followed by a black speckle pattern to facilitate displacement and strain measurements using 3D DIC system as shown in Fig. 2 (c). Three identical specimens are tested for each series considering the scattering of test results. Material properties of composite laminates are obtained by standard tensile/compressive coupon tests according to ISO [21–23] and are summarized in Table 2.

The tests are conducted by the PCX 001 Hydraulic Wedge Grip, as shown in Fig. 3, whose maximum loading capacity is 800kN for the static test and ± 600kN for the cyclic test. During the tests, the ends of braces are clamped by tailor designed clamps fixed by the hydraulic jaws of the machine to introduce load to the specimens without involvement of any welding, potentially limiting the lifetime of the test by fatigue cracks at the ends. A displacement control with loading rate of 1 mm/min is used for static tests. During the fatigue tests, all the specimens are loaded with the force range of 15-150kN (R = 0.1), while the maximum force is approximately half of the static resistance obtained in separate tests. The loading frequency is 4 Hz. Fatigue tests are stopped when stiffness degradation of the joint stabilized by less than 0.5% reduction within 5000 cycles. After that static tests are conducted to check the residual resistance of the joints. All the tests are carried out at room temperature.

GOM Aramis 3D DIC system with 12MPx cameras is positioned to acquire the displacements and local strains as shown in Fig. 3. The debonding crack propagation can be monitored in real-time and processed afterwards by analysing the strain distribution on the surface of the composite wrap [4]. During the static tests, pictures are taken at a constant frequency. During the fatigue tests, the frequency of DIC

Table 1
Test specimens.

Load type	Specimens	Loading rate/frequency	Loading range
Static	AS_1/2/3	1 mm/min	–
Fatigue	AF_1/2/3	4 Hz	15-150kN

Table 2
Material properties of the composite laminate.

Mechanical property	Average value and (CoV [%])
Longitudinal and transverse compressive modulus, $E_{x,c} = E_{y,c}$	12077.11 MPa (4.50)
Longitudinal and transverse tensile modulus, $E_{x,t} = E_{y,t}$	11798.20 MPa (6.37)
In-plane shear modulus, G_{xy}	3120 MPa (6.81)

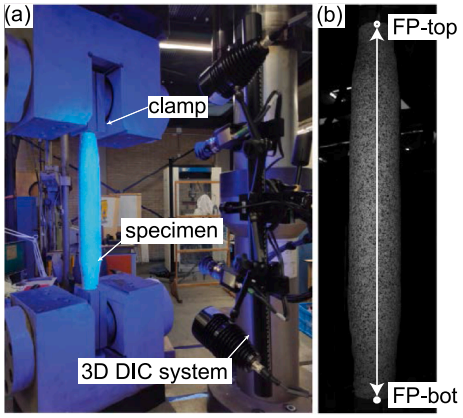

Fig. 3. Test set-up and 3D DIC system.

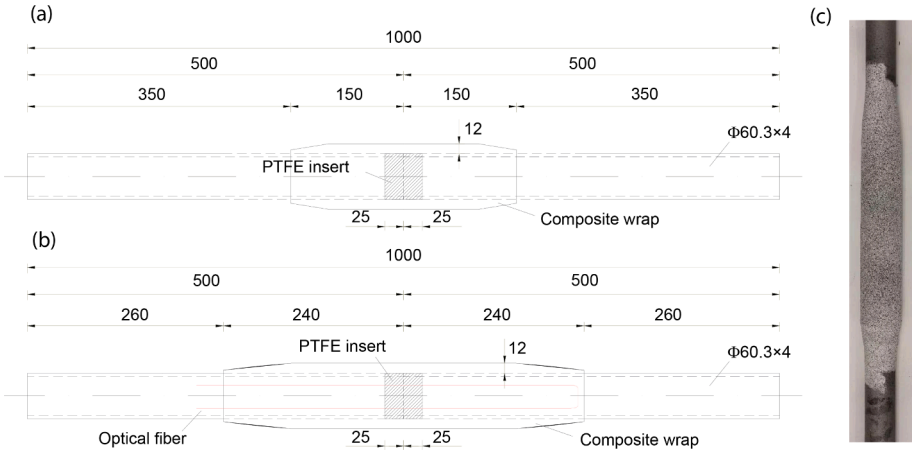

Fig. 2. Geometry and dimensions of specimens (a) static specimen; (b) fatigue specimen; (c) fatigue specimen with DIC pattern.

measurements is controlled by the testing machine. The cyclic loading is stopped every 5000 cycles or 1% of stiffness degradation, then photos are taken at the minimum and maximum forces, respectively.

LUNA ODiSI 6000 optical distributed sensor interrogator, in combination with an embedded primary coated optical fiber, is utilised to measure the longitudinal strains inside the composite. The location of the optical fibre is indicated in Fig. 2 (b) and within the first layer of the composite wrap. The LUNA interrogator uses a Rayleigh backscatter pattern which allows to measure strains with a spatial resolution up to 0.65 mm. A low bend loss optical fibre, 125 μm with Ormocer coating, is used. During the test, measurements are taken at the same intervals as the DIC measurements, controlled by the testing machine.

2.2. Static test

Relative displacement between top and bottom facet points in DIC analysis, FP-top and FP-bot, as shown in Fig. 3 are extracted for further analysis. Note that the facet points are located near the clamping ends outside of the composite wrap. Therefore, the results obtained from DIC reflect mechanical behaviour of not only wrapped joints but also part of steel tubes which is important for understanding the interaction of failure mode related to yielding of steel tube and debonding of the interface between the composite wrap and the steel tubes. Load-displacement curves of all the 3 specimens are summarised in Fig. 4. The response of the joint is analysed in detail in combination with a contour plot of strain distribution on the surface of the specimen obtained from DIC as shown in Fig. 5. In Fig. 6, strain distributions along longitudinal direction of the joint under different load levels are extracted for further analysis. The strain results are taken from one representative specimen AS _1, whose ultimate resistance, F_u, is 288kN. It can be seen from Fig. 4 that the load–displacement curves overlap with each other. The behaviour is linear before 180kN (around $0.6F_u$), representing the elastic response of the specimens. The strain distribution along the specimen peaks in the middle with the value from 0.1% to 0.4% as shown in Fig. 5 and Fig. 6 due to existence of the pre-crack. It is only the composite wrap that carries the load in this region in contrast to hybrid cross section of steel and composite in the rest of the specimen. As

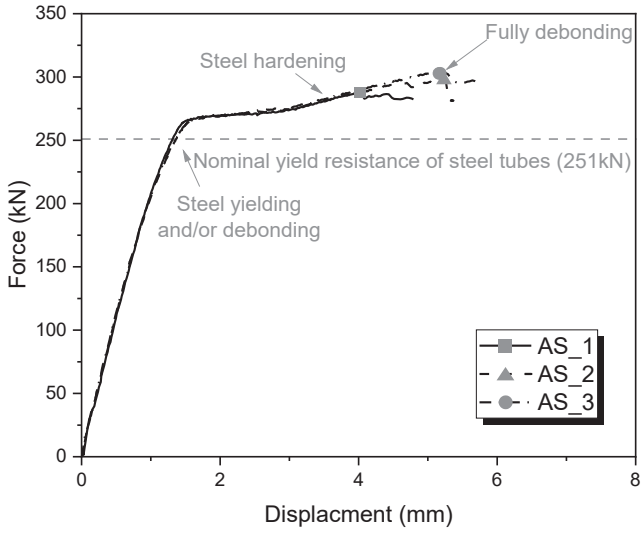

Fig. 4. Load-displacement curves of static tests.

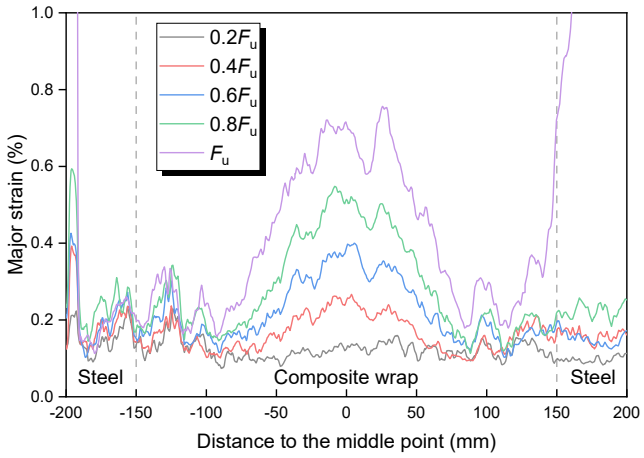

Fig. 6. Strain distribution along axis of the joint under different load levels (AS_1).

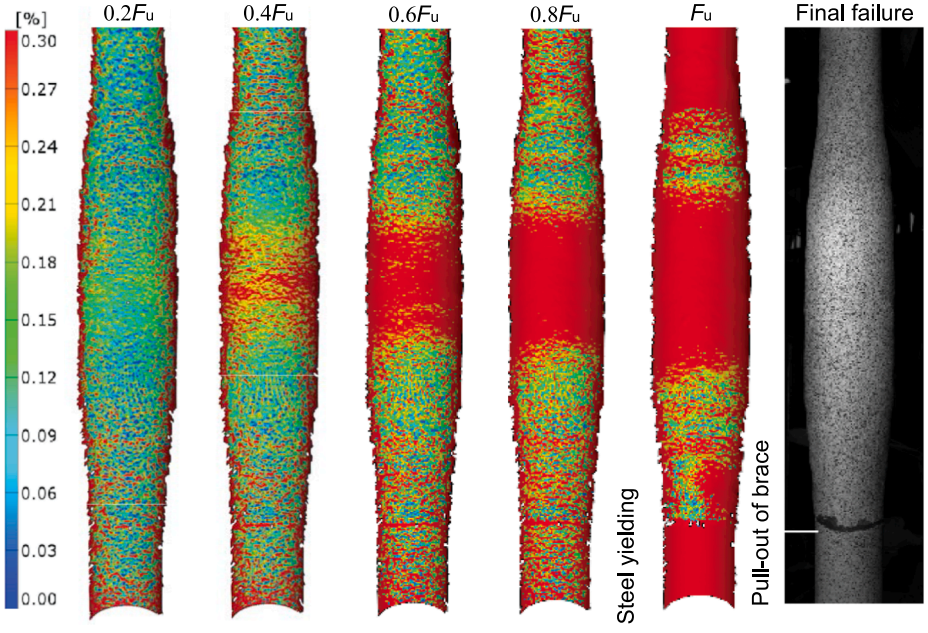

Fig. 5. Contour plot of strain distribution on surface of wrapped composite joint under monotonic load (AS_1).

Table 3
Static test results.

Specimens	K_{ini} (kN/mm)	F_e (kN)	F_u (kN)	S_e (mm)	S_u (mm)	S_u/S_e
AS _1	220.07	203.28	288.01	0.97	4.02	4.13
AS _2	217.69	184.52	298.05	0.89	5.26	5.92
AS _3	228.99	185.15	304.59	0.85	5.10	6.00
Average (CoV [%])	222.25 (2.19)	190.98 (4.56)	296.88 (2.30)	0.90 (5.56)	4.79 (11.49)	5.35 (15.97)

the load increases, the load–displacement responses become nonlinear and reach a plateau at around 270kN. This may result from steel yielding outside of composite wrap as shown in Fig. 6, where strains at the steel part under $0.8F_u$ and F_u reach the elastic strain limit 0.2%. This can also be indicated by the nominal yield resistance of steel tubes, 251kN, as shown in Fig. 4. The increasing trend of the load–displacement curves between 270kN and 300kN is attributed to steel hardening. As shown in Fig. 5, the strain increases in the middle and expands towards both sides, which could result from the combination of elastic loading, damage accumulation and debonding propagation at the interface [3,24,25]. The debonding may also lead to the nonlinear behaviour of load–displacement curves, which will be further discussed by FE models in section 3.2. It should be noted that the steel tubes may contract due to yielding outside of the composite wrap, which may cause peel stress at the composite-to-steel interface at the wrap end, leading to mode I debonding. The steel yielding and debonding behaviour will be verified through finite element analysis in the following sections. After reaching the ultimate load, the force dropped abruptly due to full debonding of one side of the joint.

The initial stiffness K_{ini}, elastic load limit F_e, ultimate load F_u, as well as their corresponding displacements S_e and S_u, and the ductility index defined by S_u/S_e of all the specimens are summarized in Table 3 for detailed analysis. The elastic load limit is determined when the secant stiffness is degraded by 5% compared to the initial stiffness. The average initial stiffness is 222.25kN/mm. The elastic load limit is lower than the nominal yield strength of the tube as indicated in Fig. 4, with the average value of F_u being 190.98kN. This may result from the fact that debonding dominates the initiation of nonlinear response before steel yielding.

2.3. Fatigue test

2.3.1. Stiffness degradation

Typical force–displacement responses of the specimen at different number of cycles are generalized in Fig. 7 (a) and one example from specimen AF _1 is shown in Fig. 7 (b). As the measurements by DIC are taken only at the maximum and minimum loads in the DIC system, no hysteretic loops can be presented but only straight lines are shown in the Fig. 7 (b). It can be seen from the figure that as the number of cycles increases, the stiffness K_i as indicated in Fig. 7 (a), defined by the load range divided by the displacement range of each cycle, decreased gradually. Dynamic secant stiffness is defined here to eliminate the influence of residual deformation on the calculated results. In such case the stiffness degradation only results from either debonding at the composite-to-steel interface or damage within the composite material [3]. The residual deformation accumulated during the test as shown in Fig. 7 (a). The residual deformation may result from fatigue-creep behaviour of the composite materials [26] which will be discussed later.

Stiffness degradation of all the specimens is summarized in Fig. 8. It can be seen from the figure that stiffness of the specimens degrade continuously during the cyclic loading. Stiffness degradation rate sees a decreasing trend for all the specimens. A major stiffness degradation (about 45%) is found within the first loading stage of 100,000 cycles. Only 10% stiffness was lost in the remaining (secondary) stage until stop of the test at around 400,000 cycles. After the fatigue tests, joints were statically loaded until failure in tension. Load-displacement curves are shown in Fig. 8 (b). The possibility for damage tolerant fatigue design of the wrapped joints is demonstrated by these results. Even with the crack propagated almost 2/3 of the original overlap length in all specimens (see section 2.3.2), the residual debonding resistance of approximately 300 kN is within the range of resistance of undamaged joints (Table 3) and surpasses the yield resistance of the steel tubes.

Stiffness degradation of the specimens may come from either debonding at the composite-to-steel interface or material damage within the composite wrap. Hypothesis is that the stiffness degradation in the presented test results is dominated by the debonding because the specimens were designed to behave in such manner to allow study of the deboning fatigue. The justification that the material damage in the tested specimens is not significantly contributing to the stiffness degradation is provided as follows. Firstly, average strain on the surface

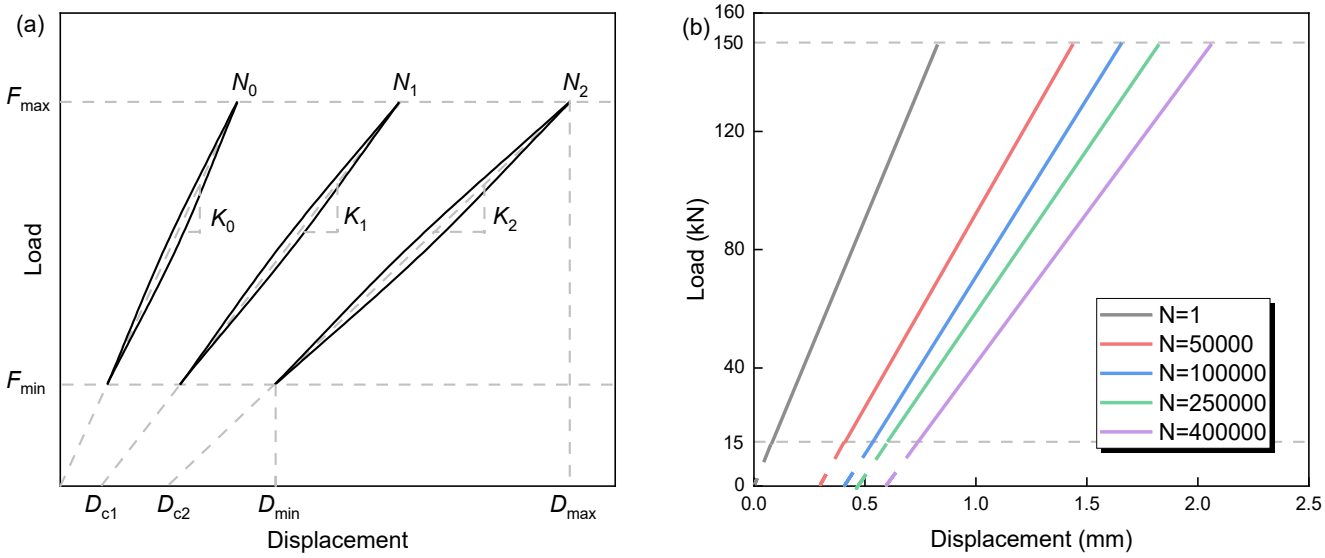

Fig. 7. Typical force–displacement curve (a) Definition of stiffness and residual deformation; (b) example from specimen AF_1.

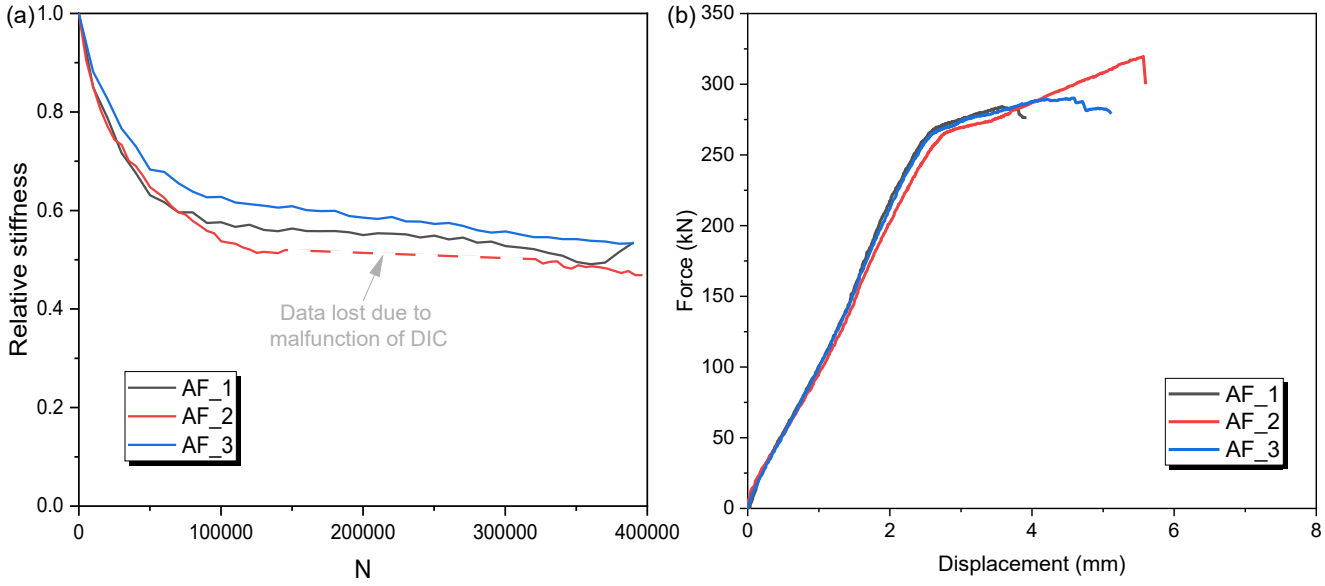

Fig. 8. Fatigue test results of A-joints: (a) stiffness degradation due to cyclic loading 15–150 kN; (b) load–displacement behaviour in static test after fatigue.

of the composite wrap within the pre-crack part (±25 mm) as shown in Fig. 9 (b), where load is mainly transferred by the composite material, is extracted through DIC system. The strain change within this region for each cycle, $\Delta\varepsilon_{ini}$, is obtained. The stress amplitude, $\Delta\sigma_{ini}$, is calculated by dividing the force range ΔF by the cross area of the composite wrap A_{cr} as shown in Fig. 9 (a). The stiffness of the composite material is then represented by $\Delta\sigma_{ini}/\Delta\varepsilon_{ini}$ and the relative stiffness degradation is summarized in Fig. 9 (a). It can be found that the average stiffness degradation of the composite material is around 10% during the whole fatigue tests. An updated elastic modulus of the composite material based on this analysis is assigned in the finite element model, which will be shown in the following sections. The results show that 10% material damage leads to only 5.5% decrease of the initial stiffness of the joint, which is negligible compared to the overall stiffness degradation of 55% as shown in Fig. 8 (a). The results indicate that stiffness degradation of the wrapped composite joints mainly comes from debonding crack propagation at the composite-to-steel interface which will be discussed in the next section.

Besides stiffness degradation, the specimens also show residual deformation during cyclic loading as shown in Fig. 7. Residual deformations of all the specimens are summarized in Fig. 10. The figure shows that specimens exhibit similar trend, namely the residual deformations develope rapidly during the first 130,000 cycles to around 0.5 mm and increase gradually up to 0.8 mm during the remaining 270,000 cycles. The maximum residual deformation corresponds to around 40% of the maximum applied displacement of 2 mm, which is not negligible. The residual deformation accumulation procedure may result from cyclic creep behaviour of the composite materials [26,27]. Creep behaviour is the time-dependent deformation under a constant load, which in this case is the average level of the cyclic loads. Important to mention is that the cyclic load level applied to the tested specimens is much higher than the expected Damage Equivalent Load (DEL) in the case of real structures, such as offshore wind turbine jacket supporting structures. Thus, the relative accumulated deformation in the full-scale joints in real structures is expected to be much less than in the presented test, even negligible. Material damage resulting from fatigue loads may

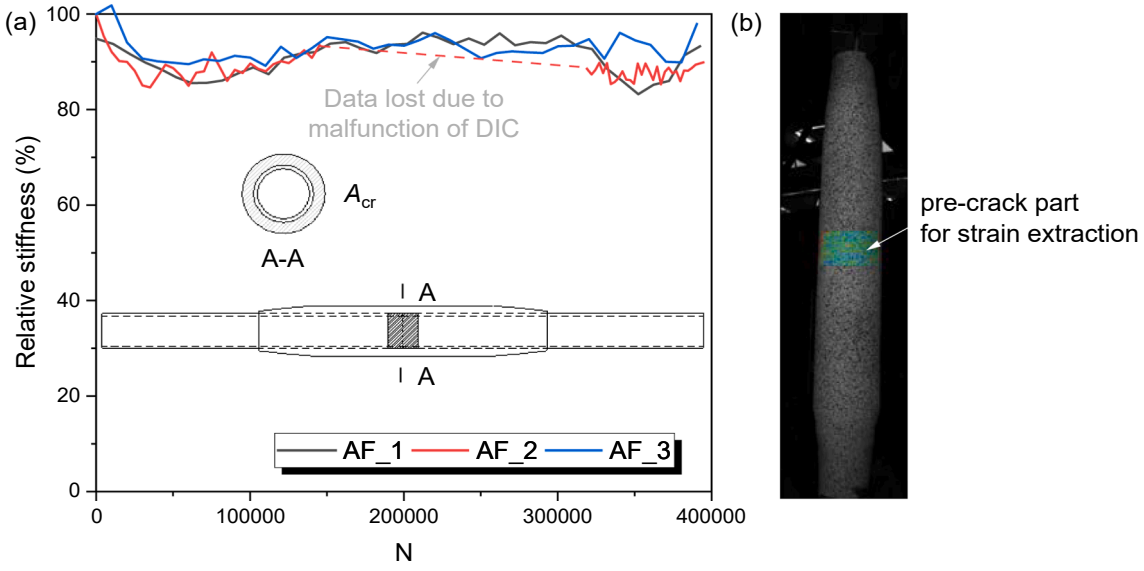

Fig. 9. Material damage check (a) stiffness degradation of composite material; (b) strain extraction at the initial crack part in DIC.

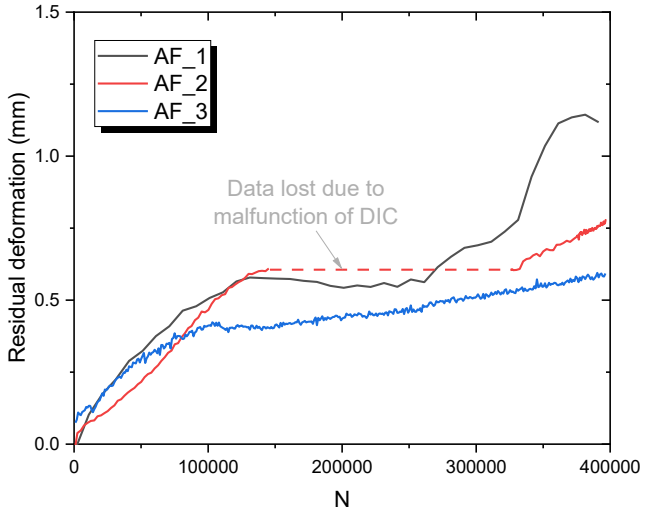

Fig. 10. Residual deformation of the joints.

increase the creep deformation. For specimen AF _1, a huge increase of residual deformation up to 1.2 mm is seen after 350,000 cycles. This may be attributed to abrupt slip or debonding and built-up debris within the specimen.

The influence of residual deformation on the calculated stiffness of the joint has been eliminated by stiffness definition as shown in Fig. 7, namely the load range divided by the displacement range. For the same purpose, the strain ranges instead of the maximum strain on the surface of the specimen are analysed to monitor the crack propagation by DIC and optical fibre measurements in the next section.

2.3.2. *Debonding crack propagation*

During and after fatigue tests, no significant surface cracks are observed in the specimens. Further inspection on strain development is conducted through DIC and optical fibre measurement systems. Fig. 11 (a) shows DIC contour plots of major strain range, namely the maximum strain minus the minimum strain, on the surface of composite wrap at different cycles. With an increasing number of cycles, the strain-increased zone (in red colour) propagates steadily from the region of the insert (pre-carrack) towards the wrapping ends, indicating debonding crack propagation at the composite-to-steel interface or within composite wrap layers. After fatigue test, namely around 55% stiffness degradation, steel tubes are pulled out of the composite wrap statically and cut into half pieces for further inspection. It can be seen from Fig. 11 (b) that the crack is propagation transfer from composite-to-steel interface to the first plies of the composite wrap at a certain location.

Strain distributions are extracted along the curves defined on the surface of composite wrap as shown in Fig. 11 (a) for further analysis. The strain ranges i.e. the difference of the strain distribution at the maximum load and the minimum load in each cycle is adopted here to eliminate the influence of residual deformation as mentioned above. The extracted strains at different number of cycles are plotted against the distance to the middle of the joint in Fig. 12 and compared with those obtained from optical fibers for specimen AF_2. It can be seen that the strains are peaked at the initial crack part in the middle, where the load is mainly transferred by the composite wrap, then decrease gradually towards both ends of the composite wrap. Different from literature [28] which shows that there is a strain plateau at the cracked part accompanied by sharp strain decrease at the bonded part, the plateau is not obvious in the current study. This may be attributed to the shear deformation gradient of such thick composite laminates, caused by restraining from the bonded part and friction at the cracked interface. Optical fibers show more rapid drop of the strains at the strain decrease region. This is because the strains from optical fibers are obtained inside the laminate close to the steel-composite interface instead of on surface of the composite wrap as in DIC. The influence of shear deformation of the wrap is smaller than in the case of DIC results. A sharper strain decrease provides more accurate information on the crack tip location. Results show that the crack length that would be determined by the optical fibres based on the strain fronts close to the interface and the crack length from the DIC system are in well agreement. Unfortunately, due to damage of the optical fibers during the test, results from Luna system experienced data loss after 35,000 cycles. For the remaining part,

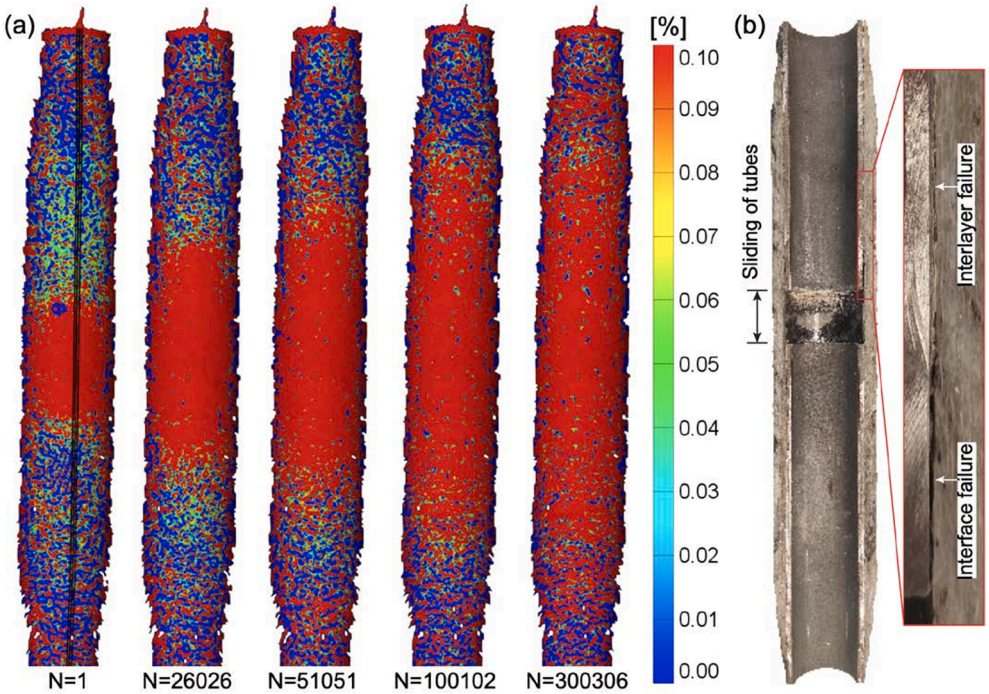

Fig. 11. Failure mode of specimens (a) debonding crack propagation at different numbers of cycles (AF_2); (b) steel tubes pulled out after static load.

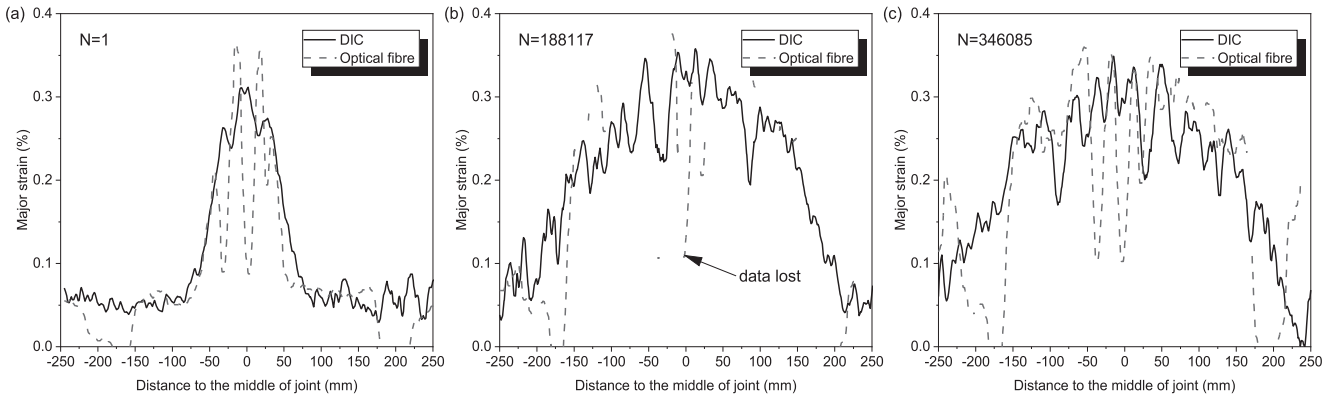

Fig. 12. Comparison on strain development from DIC and optical fiber systems (AF_2).

the strain development is only analysed by the DIC results.

Fig. 13 (a) shows strain development at different cycles taking specimen AF_3 as an example. With an increasing number of cycles, the strain fronts expand in parallel towards both ends. A constant strain threshold is taken around this region to calculate the crack increments, over which the fatigue debonding initiates. The crack lengths are calculated separately for each brace and equal to the summation of crack increments from each cycle plus the initial crack length of 25 mm. A sensitivity analysis of the strain threshold is carried out on one of these braces as shown in Fig. 13 (b), where strain thresholds of 0.1%, 0.15% and 0.2% are adopted. The results show that within the strain fronts region, the influence of adopting different thresholds is insignificant, while a higher threshold may result in scattering calculated results due to scattering and overlapping of strain distribution curves in the middle. In the following analysis, strain threshold of 0.1% is adopted for all the specimens.

The measured debonding crack propagation for all the braces are summarized in Fig. 14. For all the specimens, crack grows rapidly at early stage and sees a decreasing growth rate during the following number of cycles. Specifically, crack lengths increase rapidly from 25 mm to around 110 mm during the first 100,000 cycles, while after that the additional 40 mm crack length is achieved during the remaining

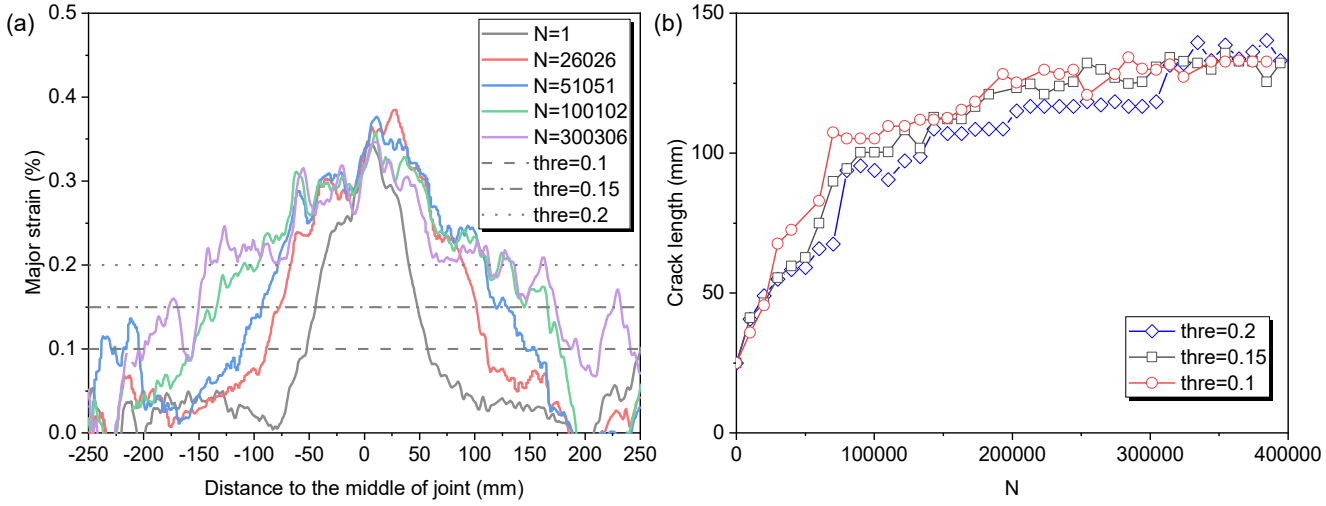

Fig. 13. Debonding crack propagation (a) Strain distribution along the specimen at different cycles; (b) debonding crack length determined by different strain thresholds (AF_3).

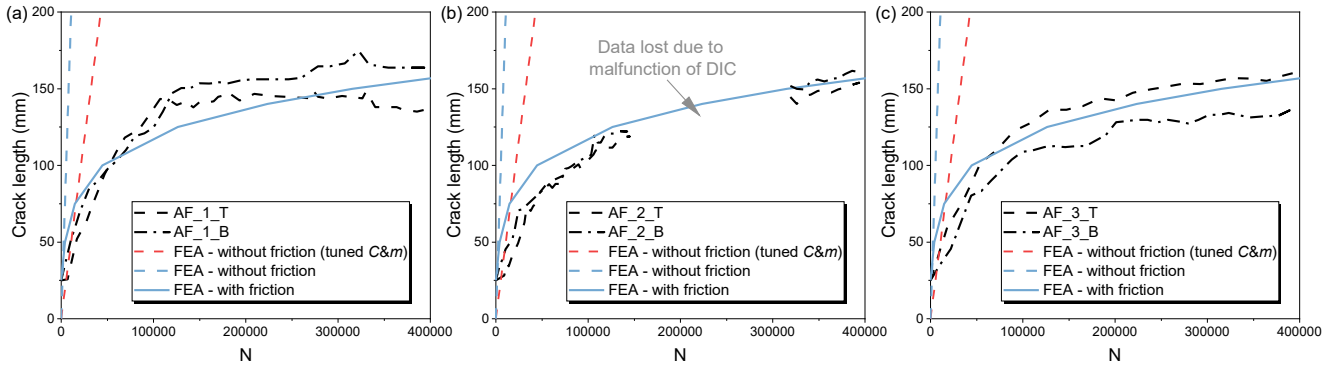

Fig. 14. Crack propagation under fatigue loads.

300,000 cycles leading to total crack length of 150 mm. In other words, crack propagation of all the specimens experienced the retardation phenomenon, exhibiting a decreasing crack growth rate. Considering that fatigue crack propagation is driven by strain energy release rate (SERR) at the crack tip according to Paris relationship [29], the crack growth retardation may be attributed to decreasing of SERR values. The contact stress between composite and steel may lead to friction effect at the interface, dissipating part of the strain energy, which is thought to be the reason of decreasing SERR values at the crack tip. Note that the fibre bridging effect may also lead to retardation of crack growth at the interface, although this effect is not predominate under mode II fatigue loading [5]. The built-up debris and micro wedge effect behind the crack tip can also contribute to friction effect, thus secondary load transfer and reduction of SERR at the crack tip. To explain this fatigue debonding retardation phenomenon due to the friction effect mentioned above, a finite element model is developed in the next sections.

3. Finite element modelling

3.1. Modelling strategy

A 3D finite element (FE) model is built in ABAQUS software [30] to interpret failure mechanisms of the tests, as well as the friction effect at the composite-to-steel interface. The geometry and dimensions of the FE model follow the design of the static and fatigue-tested specimens. The model is shown in Fig. 15. A half model is built to shorten the analysis time thanks to the symmetric character of the model. Cross section of the end of the steel tubes are coupled to a reference point, where boundary conditions are applied. All the degrees of freedom except for the U2 direction of the reference points are constraint to simulate the fixation condition resulting from clamps in the physical test. Displacement of 10 mm is applied in the U2 direction for load application with a smooth step amplitude curve. A symmetry boundary condition of U3 = UR1 = UR2 = 0 is applied on the symmetry plane. Linear, hexahedron eight-noded solid elements with reduced integration (C3D8R) are used for the steel parts, while linear tetrahedron elements (C3D4) are used for the composite wrap due to its complex geometry. A sensitivity study on the mesh size is conducted considering the dependency of strain energy release rates on the mesh size and computing efficiency. The result converges to 2 mm.

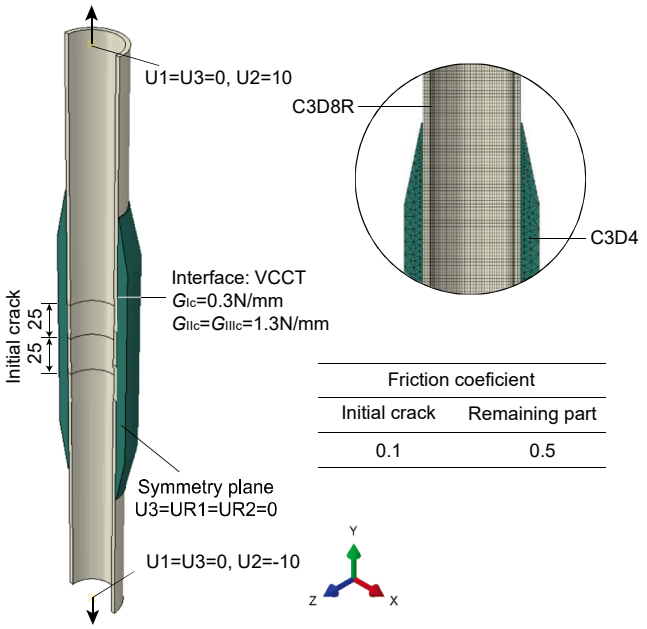

Fig. 15. 3D finite element model of the joint.

Table 4
Anisotropic elastic properties of the composite material in the model.

Elastic constants
$E_1 = E_2 = 12000$ MPa, $E_3 = 5000$ MPa, $G_{12} = 3120$ MPa, $G_{13} = G_{23} = 2500$ MPa, $\upsilon_{12} = 0.22$, $\upsilon_{13} = \upsilon_{23} = 0.3$

A linear-elastic-fracture-mechanics (LEFM)-based method, virtual crack closure technique (VCCT) [31], is utilized here to simulate the crack propagation at the bonded composite-to-steel interface and calculate the SERRs. The nodes in front of the crack tip from both steel and composite parts are coupled and will debond after the strain energy release rate (SERR) based fracture criterion, $G_T \geq G_{eqC}$, is met. For Benzeggagh–Kenane (BK) law used in this study, G_T represents the total SERR, i.e $G_T = G_I + G_{II} + G_{III}$. G_{eqC} is the equivalent critical SERR, which is defined by:

$$G_{eqC} = G_{IC} + (G_{IIC} - G_{IC})\left(\frac{G_{II} + G_{III}}{G_T}\right)^{\eta} \quad (1)$$

where G_{IC} and G_{IIC} are the critical mode I and mode II SERRs, and $\eta = 1.8$. The initiation values of critical SERRs, i.e. $G_{IC} = G_{I,ini} = 0.3$ N/mm and $G_{IIC} = G_{IIIC} = G_{II(III),ini} = 1.3$ N/mm, are used as the criterion which are obtained through standard DCB and ENF test according to **Ref.** [32]. Two methods are attempted to simulate the possible friction effect as the crack progresses at the interface. The first one is to tune the critical SERR between the initiation and the propagation values ($G_{I,prop} = 1.1$ N/mm and $G_{II,prop} = G_{III,prop} = 3.5$ N/mm) until the force–displacement curve reaches a good match with the experimental results. The second method is to directly define friction at the cracked interface in combination with VCCT crack propagation based on initiation value of critical SERR. The friction coefficient is measured by a tribometer, which is found to be 0.1 at the insert part between composites and steel and to be 0.5 at the bonded part. The modelling procedure is validated not only by comparing force–displacement curves with the static tests but also the strain distribution on the surface of the composite wrap from the cyclic load experiments obtained by DIC, which will be discussed in the next section.

Plasticity model in ABAQUS is used in this study to model non-linear behaviour of steel. Elastic constants (E = 210GPa, and υ = 0.3) and nominal yield and ultimate stress (S355, $f_y = 355$ MPa, $f_u = 510$ MPa) in combination with isotropic hardening are used for the steel tubes. The composite wrap is modelled as one piece of solid part in this model. Stresses in the composite wrap in the ultimate load (static) and cyclic load (fatigue) tests are much lower than the strength of the material shown in Table 2. Therefore, the composite wrap is modelled with elastic material properties. Transversely anisotropic material properties are defined based on the tests results shown in Table 2 for the in-plane properties of the laminate: E_1, E_2, G_{12} and υ_{12}. In absence of test data, the out-of-plane elastic properties of the laminate E_3, $G_{13} = G_{23}$, $\upsilon_{13} = \upsilon_{23}$ are defined based on values obtained through Classical Laminate Theory for an equivalent unidirectional material with the fibre volume fraction conforming of the tested laminate ($V_f = 30\%$). The elastic constants used are shown in Table 4.

3.2. Results of modelling the static experiments

The simulated force–displacement curves for ULS analysis are plotted versus test results in Fig. 16 (a). All the FE modelling results are overlapped with each other at the linear elastic stage and non-linear stage until 275kN and match well with the test results. This is because that the nonlinearity of the force–displacement response until this stage mainly reflects yielding and hardening behaviour of the steel tubes outside the composite wrap, accompanied by relatively short, up to 6 mm, debonding at the interface. Whereas the ultimate loads, which correspond to fully debonding at the interface, vary among different FE

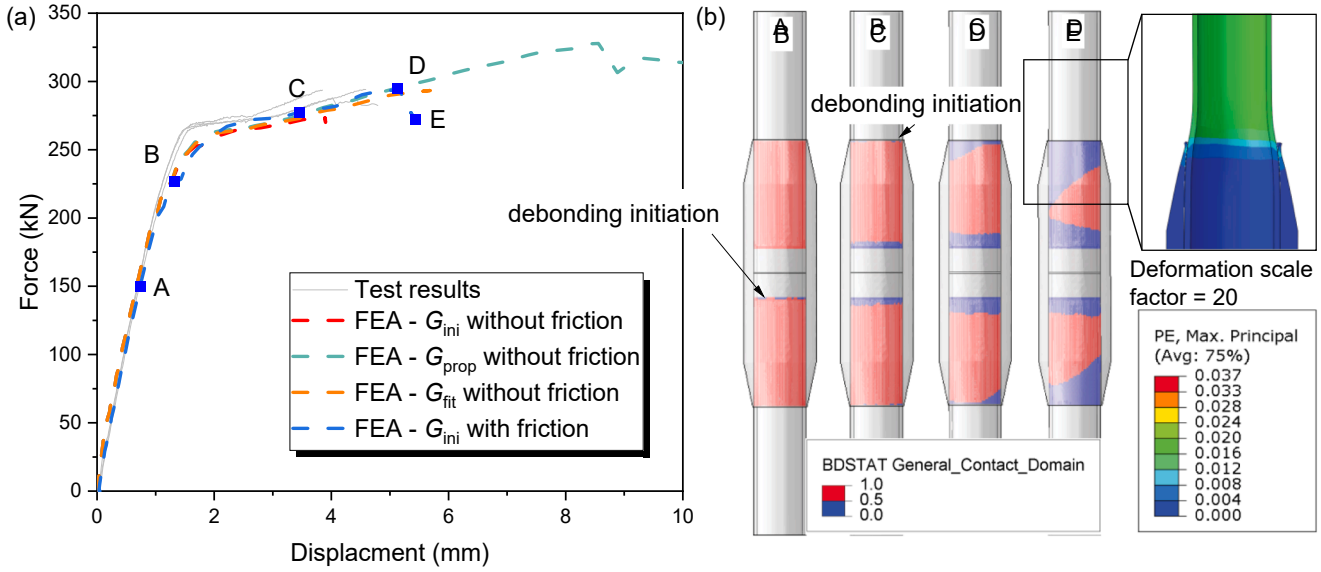

Fig. 16. Modelling results (a) force–displacement curves; (b) crack debonding process.

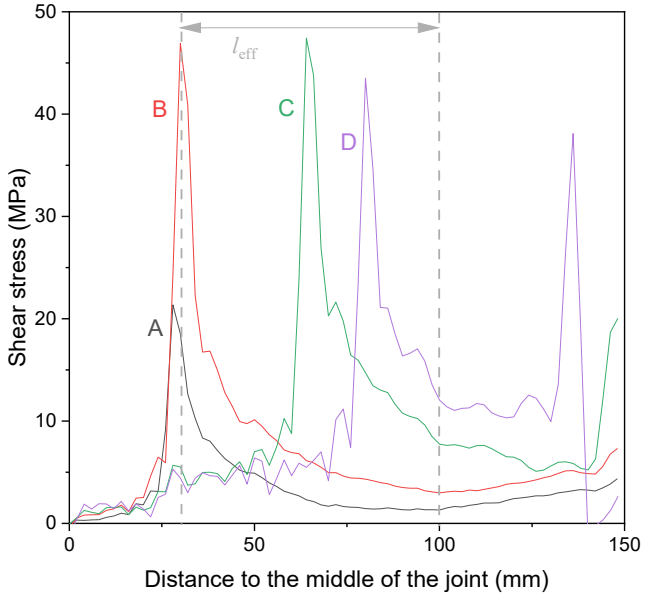

Fig. 17. Shear stress distribution at the interface for different loading stages.

models. For the first modelling methodology, i.e. model with adjusted critical SERRs, the initiation values ($G_{I,ini} = 0.3$ N/mm and $G_{II,ini} = G_{III,ini} = 1.3$ N/mm) and propagation values ($G_{I,prop} = 1.1$ N/mm and $G_{II,prop} = G_{III,prop} = 3.5$ N/mm) of SERR are tried firstly. The model with the initiation value of SERR underestimates the ultimate load while model with the propagation value of SERR overestimates the ultimate load and deformation drastically. In the next step, the critical SERR values are calibrated between the initiation and propagation value until the good match with the test results was found. The best fitted model is found to have the critical SERR values of 0.4 N/mm for mode I and 2.2 N/mm for mode II, respectively. For the second methodology, i.e. model with friction defined at the interface, the force–displacement curves as well as the strain distribution curves also match well with the test results as indicated in Fig. 16 and Fig. 17, respectively. Although the first method can also reach a good match in terms of force–displacement, the strain distribution along the surface of the composite wrap doesn't match the test results as shown in Fig. 17 (a) when friction is not considered in the model. Meanwhile, the friction defined in the second method can efficiently explain the crack retardation phenomenon which will be discussed later. Therefore the second method is adopted during the following analysis.

Stages of debonding obtained from the FE model with friction defined at the interface is shown in Fig. 16 (b). The debonding crack initiates at the inner side of the bonded interface at the force level of 250kN (point B). After crack propagates by 6 mm at the inner side, a secondary crack initiates at the outer side, namely the wrapping ends, at the force level of 275kN (point C). The secondary crack initiates due to steel yielding outside of the wrap, which leads to contraction of the steel tubes and peel stress at the composite-to-steel interface as shown in Fig. 16 (b). After the peak load of 290kN (point D), cracks at the inner side and the outer side further develop until merging with each other, resulting in full debonding at the interface (point E) and load drop.

The shear stresses at the interface are extracted for different loading stages as shown in Fig. 17. It shows that the shear stresses concentrate around the crack tip and gradually decrease towards the wrapping end. At the elastic loading stage A, the peak shear stress is only 20 MPa. When the crack initiates at stage B, the shear stress at the crack tip reaches the maximum value of 47 MPa. After that the peak stress moves towards to the wrapping end until reaching stage C, where a secondary crack initiates at the end. As the shear stresses are shared by two crack fronts from the stage on, the peak stresses start to decrease. According to this figure, the effective bond length is around 70 mm. It should be noted that outside the effective bond length, the shear stresses can arise due to friction in front of the crack tip, which may further contribute to the bearing capacity of the joint. In such case, the force can further increase and no constant loading stages are observed as in literature [33,34]. Full debonding happens when the force increases to the bearing capacity at stage D.

3.3. Results of modelling the fatigue experiments

3.3.1. Strain distribution on the composite wrap

Models of fatigue tested specimens with stationary cracks of different lengths are loaded in a quasi-static manner until the maximum force level during fatigue tests, i.e., 150kN. The strain distribution ranges on the surface of the composite wrap are validated against the corresponding test results as shown in Fig. 18 (a). Friction at the interface is or isn't considered to highlight the rationality of its existence. As shown in this figure, strain distributions from the models with friction resemble well with the test results of corresponding crack lengths. The strain

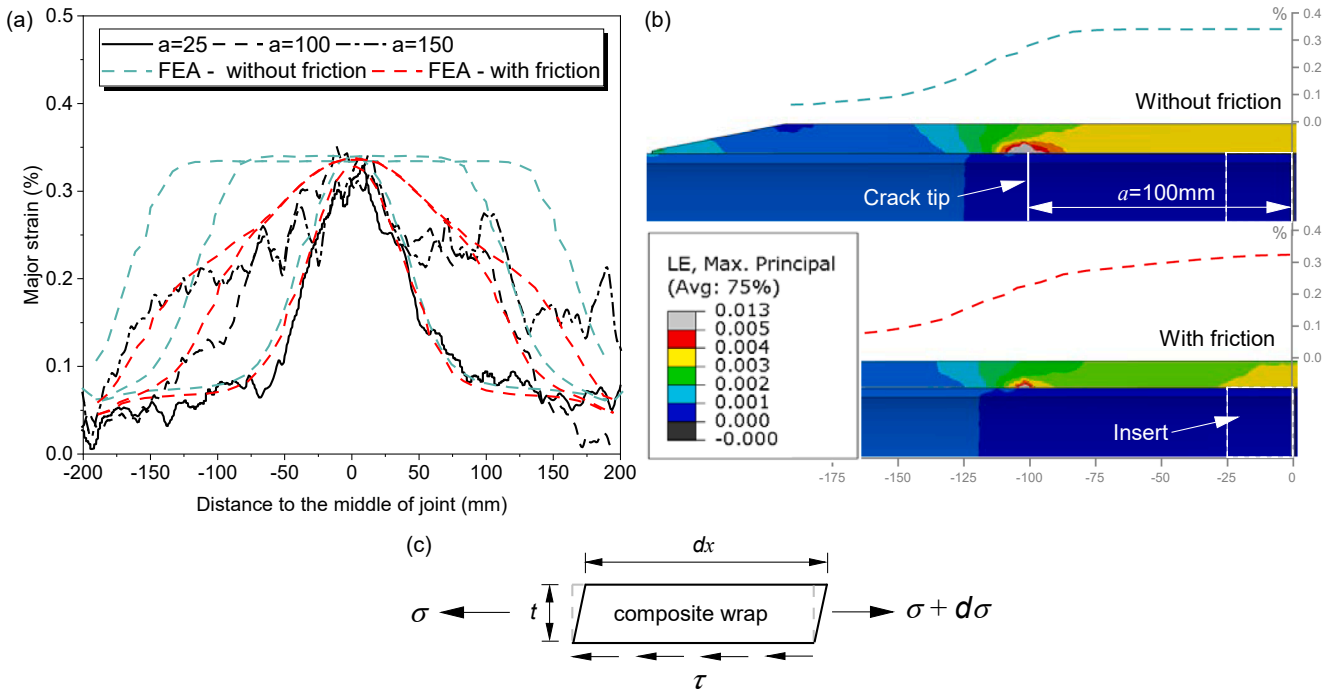

Fig. 18. Major strain distribution in the composite wrap (a) strains at surface from experiments and FE models (along the length, x = 0 mm at connection of two tubes); (b) strain distribution from the FE models in the longitudinal cut through the composite wrap and the steel tube; (c) equilibrium of an infinitesimal element of composite wrap with restraint at the interface.

distribution follows a typical bilinear shape for each side of the joint, where the strain gradient at the cracked part shows a smaller slope than that at the bonded part. Whereas for models without friction, strain distribution at the cracked part exhibits a plateau. The reason behind the difference is explained with reference to Fig. 18 (b) and the equilibrium of an element of the composite wrap in Fig. 18 (c). The equilibrium is expressed in Eq. (2):

$$d\sigma = \frac{\tau}{t} dx \tag{2}$$

where σ and τ are the tensile stress in the composite wrap and shear stress at the interface, t is the thickness of the wrap, x is the coordinate in the longitudinal direction. τ can either result from bond between composite and steel, or friction at the debonded interface. In an idealistic case without the friction at the cracked interface ($\tau = 0$), the strains in the composite are constant (the stress gradient $d\sigma/dx = 0$) is observed because it is only the tubular cross section of the composite wrap that transfers the axial load. On contrary, in the case with the friction defined ($\tau \neq 0$), the deformation of the composite wrap at the cracked part is partially restrained by the friction at the interface. Therefore, a portion of the axial load is transferred to the steel cross section in the debonded region, leading to the non-constant strain distribution in the composite wrap (the stress gradient $d\sigma/dx \neq 0$) in the debonded region. Restraint from the bonded interface is more significant, resulting in a larger slope of strain gradient (strain front) on the surface of the composite wrap. The strain front at the bonded part at different number of cycles again is parallel to each other from the FE results, providing the rationality of using a constant strain threshold within this region (0.1%-0.2%) to determine the crack length as discussed in the section of 2.3.2.

3.3.2. *Crack propagation and stiffness degradation*

When multiple energy dissipation mechanisms exist at the interface, the crack propagation follows the Paris relationship interpreted in terms of SERR values at the crack tip G_{tip} [13,35]. SERR values at the crack tips of different locations are extracted for further analysis of the influence of friction effect on the crack propagation. SERR values of different modes are extracted at the crack tip for the FE model with the initial crack of 25 mm corresponding to the PFTE insert as shown in Fig. 19 (a). The figure illustrates that mode II SERR is dominating, which is to be expected for such in-plane shear behaviour at the composite-to-steel interface. This is because the cylindrical shape of the interface prevents the radial deformation of the composite wrap and therefore eliminates the peel stresses. The average mode II SERR values at different crack lengths are obtained for FE models with and without friction applied as shown in Fig. 19 (b). It can be seen that when the friction is applied, the mode II SERR decreases from 0.85 N/mm to 0.24 N/mm as the crack length increases from 25 mm to 150 mm. Without the friction being applied in the cracked region, the mode II SERR is fairly constant. This is because the composite wrap is solely transferring the applied constant force, see Fig. 18 (b), and the thickness of the composite is constant, therefore the stresses around the crack tip are the same for all the crack lengths from 25 mm to 150 mm. However, in presence of friction the force in the cross section of the composite wrap near the crack tip reduces because larger and larger portion of the force is being transferred to the steel tube by the friction as the crack grows. The reduced force in the cross section of the composite wrap results in reduction of stresses and strains in the composite at the crack tip and therefore decreased SERR. The SERR curves with and without friction are fitted in Fig. 19 (b) with second order polynomial functions for further analysis.

With the SERR development calculated, the crack growth at the composite-to-steel interface can be predicted based on the Paris relationship, as shown in **Eq.** (3).

$$da/dN = C(\Delta G_{tip})^m \tag{3}$$

An accompanying study is conducted to obtain the Paris relationship parameters through cyclic End Notch Flexure (ENF), 4-point bending tests on steel-composite coupons, which is out of scope of this paper. FE models of coupons with varying crack lengths are employed to obtain SERRs in ENF test to ensure that the resulting Paris relationship is comparable to the SERR obtained in the joint models. The preliminary Paris relationship parameter C is found to be in the range of 0.01–0.03 and the parameter m in the range of 2.5–4, respectively. Based on the

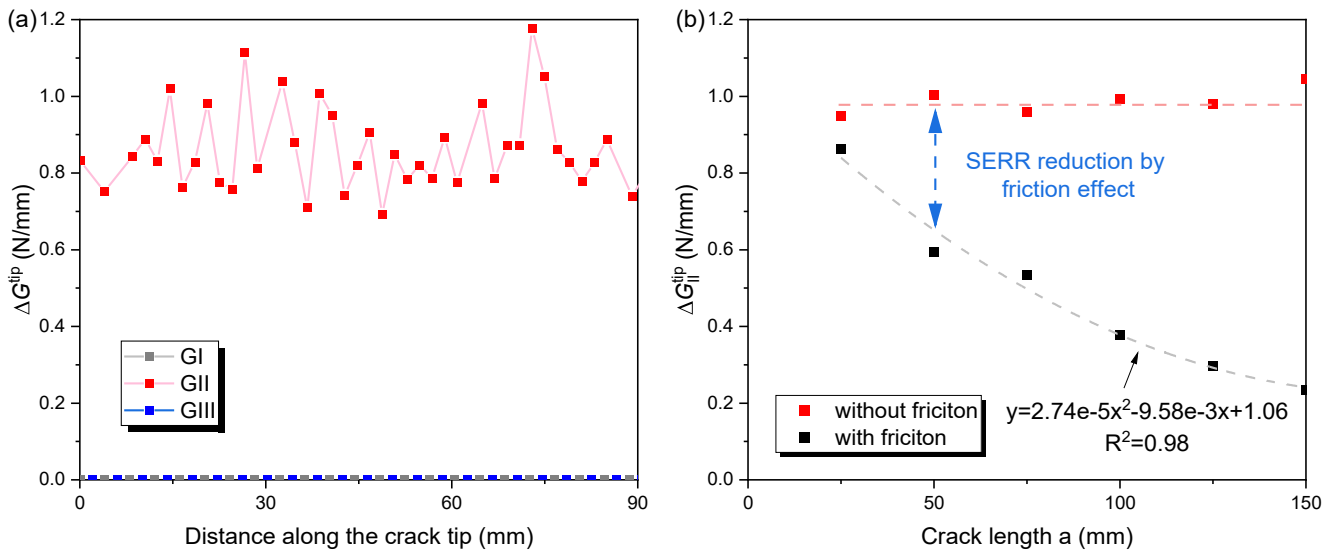

Fig. 19. SERR values (a) distribution along crack tip; (b) development with crack growth.

obtained Paris relationship parameters and regression of crack tip SERR versus crack lengths as shown in Fig. 19 (b), the number of cycles corresponding to a certain crack length can be calculated based on **Eq. (4)**. Predicted crack growth are plotted together with the test results as shown in Fig. 14 and comparisons are made to the different joint specimens that were tested. The figures show that without consideration of friction effect, the predicted crack growth only matches with the test results in the initial stage even when the best tuned C and m parameters (C = 0.005, m = 4) are adopted (dash red lines). But the crack growth is significantly overestimated with relatively high constant crack growth rate at later stages. Whereas predicted results with friction effect taken into account exhibit a typical retardation phenomenon, which agree much better with the test results when adopting the best tuned combination of Paris relationship parameters of $C = 0.02$ and $m = 3.75$within experimentally obtained ranges. For comparison reasons, the predicted results without friction with the same C and m values are also shown in the figure (dash blue lines), which obviously overestimate the crack growth.

$$N = \int_{a_0}^{a_N} \frac{1}{C[\Delta G_{tip}(a)]^m} da \tag{4}$$

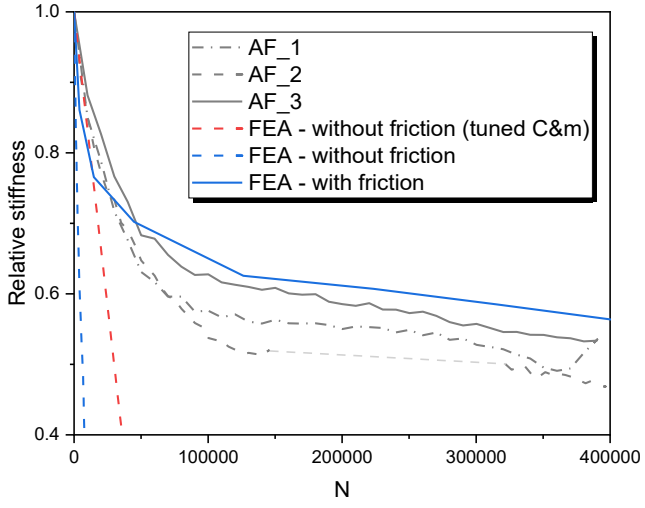

Fig. 20. Prediction on stiffness degradation.

Stiffness degradation predicted by FE models with different crack lengths are plotted against the number of cycles and compared with test results as shown in Fig. 20. It is shown that similar to the test results, the predicted stiffness degradation curve with friction considered drops rapidly, i.e. 35% is lost within the first 150,000 cycles. After that a stabilization trend is seen and additional 10% of the initial stiffness is lost during the remaining 250,000 cycles. On the contrary, the model without friction overestimates the stiffness degradation a lot, where 60% stiffness degradation is lost within just 10,000 cycles (dash blue lines). Again, even when the best tuned C and m parameters ($C = 0.005$, $m = 4$) is adopted for the model without friction, the predicted results can only match well with the initial stiffness degradation but overestimate it at later stages.

The model with friction and Paris relationship parameters of $C = 0.02$ and $m = 3.75$ underestimates the stiffness degradation obtained in tests. Possible reasons could be that: 1) the prediction doesn't take into account the material damage; 2) there might be errors and unconsidered scattering in the preliminary ENF test due to limited number of specimens.

4. Parametric study of fatigue crack growth

The sensitivity of fatigue behaviour to the governing parameters of the FEA validation, namely friction coefficient, crack location (depth), and Paris relationship parameters C and m is investigated in this section. The damage tolerance up to 50% stiffness degradation has been demonstrated in the fatigue experiments, see section 2.3.1, which correspond to crack length of 150 mm, i.e. 2/3 of the original overlap length. For the comparisons in this parametric study a more rigorous failure criterion, i.e. 30% stiffness degradation, is used to determine the number of cycles to failure.

4.1. Influence of friction coefficient

As the retardation phenomenon is caused by the friction effect at the interface, the utilized friction coefficient μ has a great influence on the predicted results. The physical reasoning behind varying value of the friction coefficient are variations of the surface roughness, amount of fiber bridging and built-up debris etc. In the current study, the friction coefficient at the cracked part is varied from 0.3 to 0.7 to investigate its influence on the SERR development and crack propagation and retardation. Note that the friction coefficient at the initial cracked part remains unchanged as 0.1 considering that the friction coefficient of this

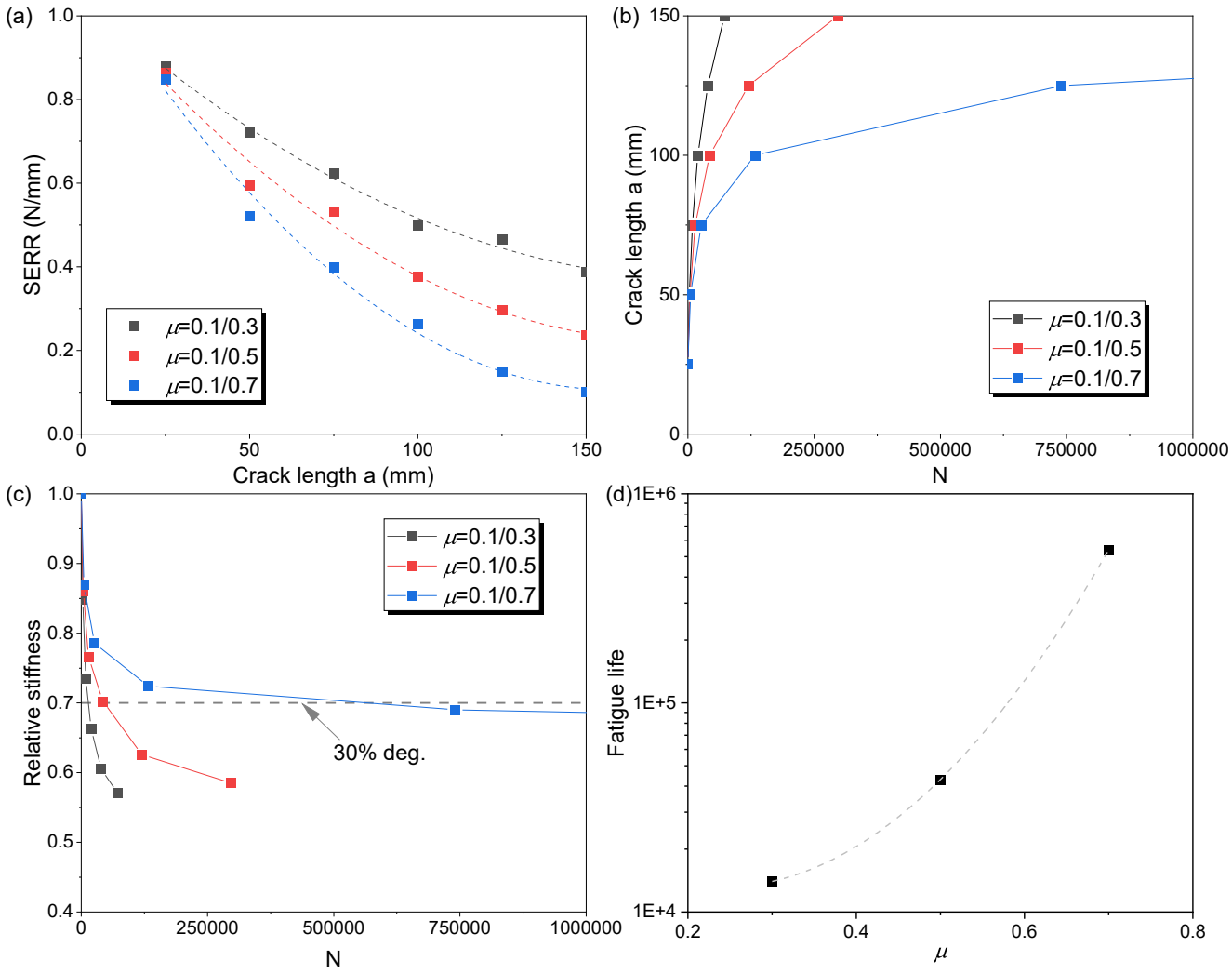

Fig. 21. Influence of friction coefficient on (a) SERR development; (b) crack growth; (c) stiffness degradation; (d) fatigue life vs. friction coefficient.

part is only influenced by the PTFE insert.

SERR development vs. crack growth from models with different friction coefficients are plotted in Fig. 21 (a). It can be seen that starting from the same level, i.e. 0.85 N/mm, SERR values with higher friction coefficient decreases more as the crack grows. For instance, SERR value of model with friction coefficient of 0.7 has dropped by 88% to 0.10 N/mm as the crack increases from 25 mm to 150 mm, while the same value from model with friction coefficient of 0.3 only drops by 56% to 0.39 N/mm. 2.3 times higher friction coefficient leads to 53% higher SERR decrease. Based on **Eq.** (4), the fatigue crack growth curves can be obtained as Fig. 21 (b). The results show that model with higher friction coefficient exhibits more obvious crack growth retardation phenomenon. According to Paris relationship, 2 times increase of SERR may lead to $(2)^{3.75} = 13.5$ times higher crack growth rate, which is the slope of crack growth curves in Fig. 21 (b). Stiffness of different models are normalized against the initial value and plotted versus the obtained number of cycles from **Eq.** (4). As shown in Fig. 21 (c), higher friction results in more significant stiffness stabilization in the later loading stages. Taking 30% as failure criterion, the relationship between fatigue life and friction coefficient is shown in Fig. 21 (d). the model with friction coefficient of 0.7 may have 39 times longer fatigue life than that with friction coefficient of 0.3 (540,000 vs. 14,000 cycles). This means that if the surface is rough enough, the crack growth at the debonded interface may be totally arrested. The other failure modes such as material failure may take place. Further study needs to be conducted to correlate the friction coefficient to cracked surface roughness parameters, such as R_z [3], to give better design recommendations.

4.2. *Influence of failure modes (crack location)*

As shown in Fig. 11 (b), there are still remaining laminates on the steel surface after the tubes are pulled out, which means that the crack may exist within the composite layers (delamination) instead of composite-to-steel interface (debonding), or transfer from debonding in the beginning to delamination during later stages as illustrated in Fig. 22**.** In this section, the influence of failure modes on SERR development, crack growth, as well as stiffness degradation is investigated. To simulate the delamination case, the composite wrap is modelled as 2 separate parts. A 1.05 mm layer of laminate is tied with the steel surfaces, while the interface with VCCT and friction is defined between the thin laminate and the remaining composite part. The friction coefficient is kept as the reference values, namely 0.5.

The results are summarized in Fig. 23. Due to existence of the insert, the crack must initiate at the composite-to-steel interface. That's why the SERR values at the initial crack length coincide with each other for the debonding and delamination cases as shown in Fig. 23 (a). As the crack propagates into the composite layers, the interlaminar SERR values are 10–20% lower than those at the interface at crack lengths of 50–100 mm but become similar to those values at longer crack lengths of 125–150 mm. As the SERR values are determined by the stress state

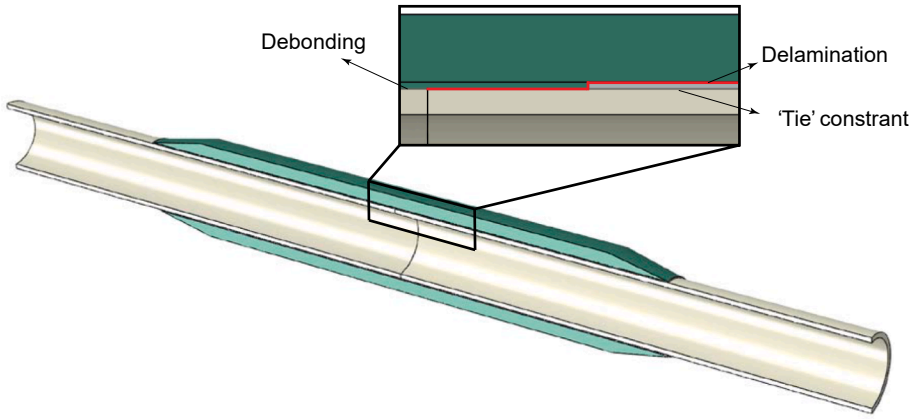

Fig. 22. Failure mode transformation from debonding to delamination.

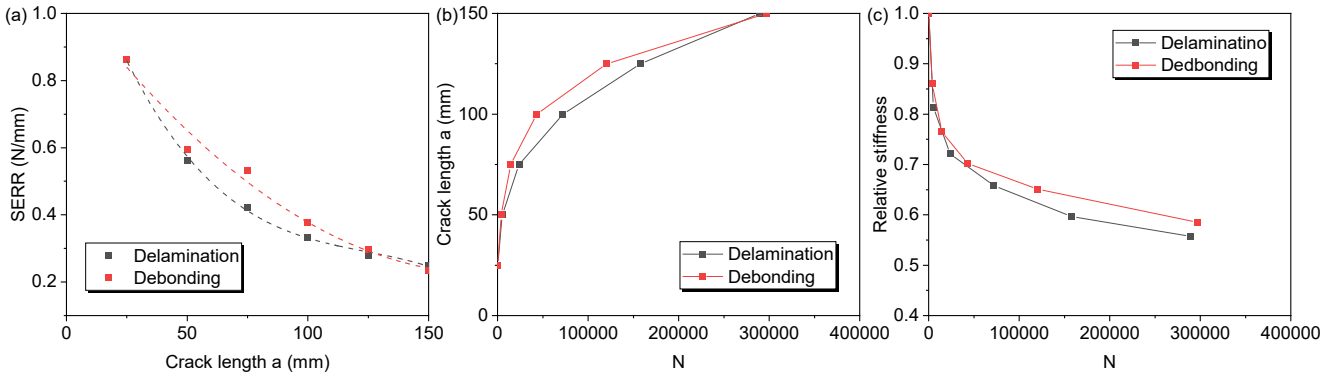

Fig. 23. Influence of failure modes (a) SERR development; (b) crack growth; (c) stiffness degradation.

around the crack tip, the shear stresses at interlaminar (for delamination case) and interface (for debonding case) are extracted at a = 75 mm and a = 150 mm for further interpretation as shown in Fig. 24. It is found that at 75 mm, shear stresses around the crack tip are higher at the interface than those between composite layers, which may come from the stress singularity at the bi-material interface. As the crack grows, stresses around the crack tip decreases as more force is transferred by friction at the cracked part. The difference between debonding and delamination cases also vanishes possibly due to diminishing of stress singularity at the interface resulting from lager friction effect. For the sake of comparison the same preliminary Paris relationship is considered at the delaminated interface inside the first layer. The crack growth

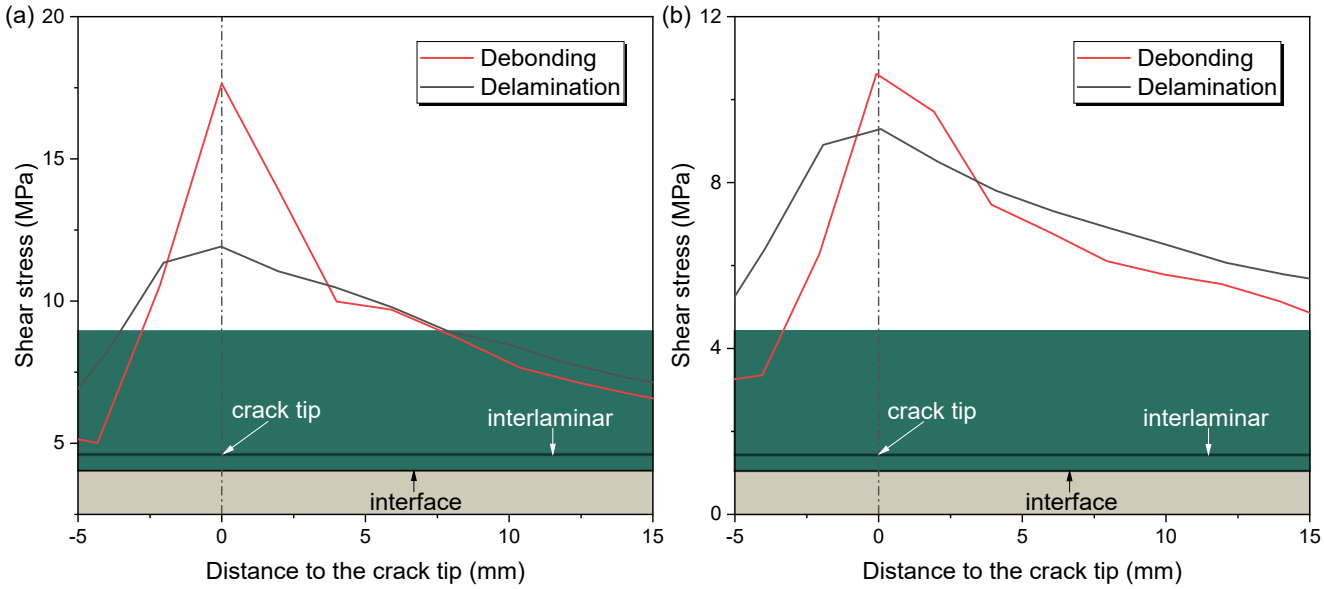

Fig. 24. Shear stress at the interface for debonding vs. interlaminar for delamination (a) for crack length of 75 mm; (b) for crack length of 150 mm.

is predicted as in Fig. 23 (b). With higher SERR values, debonding crack shows a higher growth rate around 100 mm but becomes closer to the delamination crack at later stages. The stiffness degradation of these two cases is shown in Fig. 23 (c) and is close to each other until 30% stiffness degradation. The deboning case exhibits a less stiffness degradation at later stages as the joint shows a higher stiffness with the same crack length compared to the delamination case. Taking the 30% stiffness degradation as the failure criterion, model with delamination failure has a similar fatigue life as the model with debonding failure (both around 43,100 cycles).

4.3. Influence of Paris relationship parameters

Paris relationship parameters, C and m which are obtained through fatigue ENF tests, are stochastic parameters influenced by surface preparation, fibre volume fraction, level of cure, etc. As the Paris relationship parameters used in this study are obtained based on preliminary ENF tests, the influence of Paris relationship parameters on the predicted results are discussed here. Among these two parameters, parameter C determines the position (higher or lower) of Paris relationship curve. A higher C value means more rapid crack propagation. Herein C is varied between 0.01 and 0.03, while the friction coefficient is kept as 0.5. It can be seen from Fig. 25 (a) that with higher C values, crack length increases more rapidly. It takes around 630,600 cycles for model with $C = 0.01$ to reach crack length of 150 mm, while it takes only 210,200 cycles to reach the same crack length when C is equal to 0.03. Despite the non-linear effects introduced by the friction, relationship between the crack growth and C value at constant amplitude load seems to remain linear as defined per Paris relationship in **Eq.** (3). The stiffness degradation curves are shown in Fig. 25 (b). Obviously, a higher C value corresponds to a higher stiffness degradation rate. Taking 30% stiffness degradation as the failure criterion, the relationship between fatigue life and C value is obtained in Fig. 25 (b). An roughly inverse linear trend is shown in this figure, namely, model with $C = 0.01$ shows 3 times longer fatigue life than model with $C = 0.03$ (89,450 vs. 29,800 cycles).

The other parameter m determines the slope of the Paris relationship. As the SERR values are always below 1 in this study, as shown in Fig. 19, a higher m value with constant C parameter may lead to a lower crack growth rate. Herein the m value varies between 2.5 and 4, while the parameter C is kept constant as 0.02. As shown in Fig. 26 (a), It takes around 97,600 cycles for model with $m = 2.75$ to reach crack length of 150 mm, while it takes 315,300 cycles to reach the same crack length when m is equal to 3.75. The same trend goes for stiffness degradation. Taking 30% stiffness degradation as the failure criterion, the relationship between fatigue life and m value is obtained in Fig. 26 (c). A linear trend is shown in this figure, namely, 18% increase of m from 2.75 to 3.25 leads to 43% increase of fatigue life (around 21,655 to 30,960), while 16% increase of m from 3.25 to 3.75 leads to 45% longer fatigue life (around 30,960 to 44,725).

4.4. Limitations of the parametric study

Through the parametric study, influence of several parameters on the predicted crack growth and stiffness degradation of wrapped composite joints have been investigated. Good agreement with crack propagation in fatigue experiments is found. However, there are limitations. For instance, only debonding/delamination is considered as the failure mode here. When the friction coefficient is large enough, the crack growth at the debonded interface may be totally arrested due to very low SERR values. Other failure modes such as material damage or fracture may take place during fatigue loadings. Secondly, the delamination failure and debonding failure mechanisms are investigated separately in

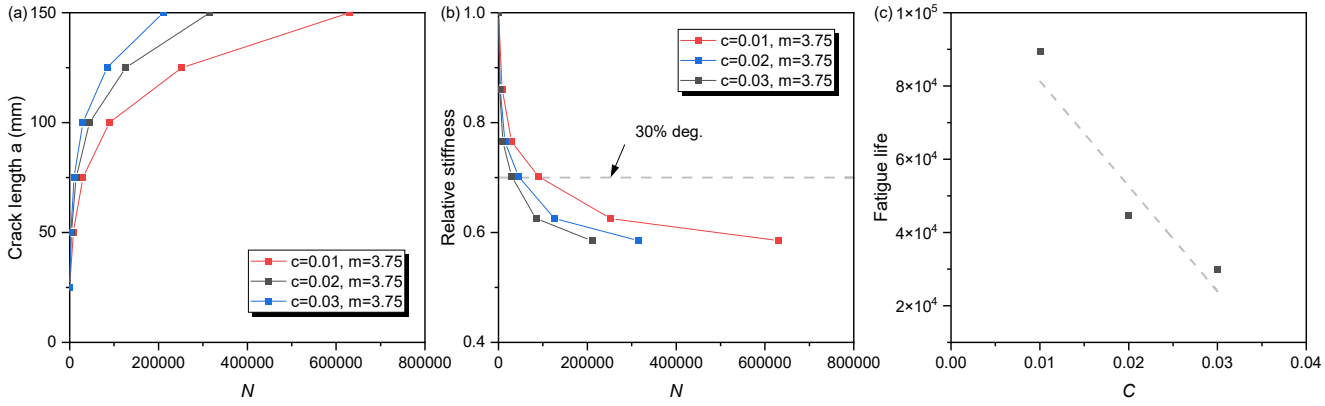

Fig. 25. Influence of C parameter on (a) crack growth; (b) stiffness degradation.

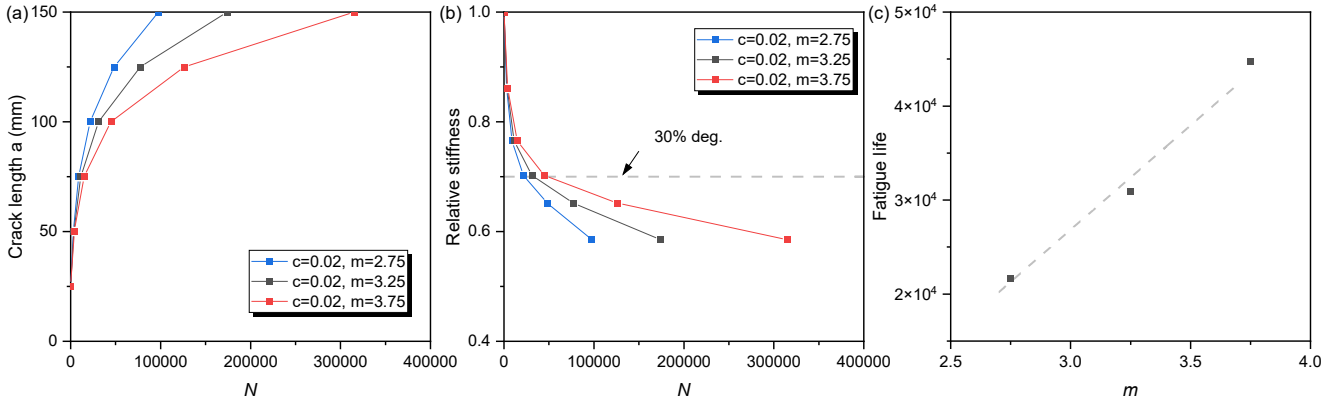

Fig. 26. Influence of m parameter on (a) crack growth; (b) stiffness degradation.

this study. They may interact and there might be transition between these two failure modes at a certain crack length. Furthermore, the Paris relationship used in this study was obtained from fatigue ENF test which showed debonding failure at the composite-to-steel interface. Paris relationship for crack growth within composite layers may differ. Finally, the predicted results are sensitive to the Paris relationship parameters, especially parameter m as discussed in section 4.4. More fatigue ENF test should be carried out to support this kind of analysis.

5. Concluding remarks

Crack retardation phenomenon in fatigue experiments on wrapped composite joints is found and explained based on experiments and FE modelling. The influence of friction effect on the debonding crack propagation at the composite-to-steel interface of wrapped composite joints is thoroughly investigated. Static and fatigue experiments are conducted on the uniaxial small-scale joints, where 3D DIC and optical fiber systems are used for monitoring crack propagation and stiffness degradation. The results are interpreted by 3D finite element model using VCCT to obtain the SERR at the crack tips. After being validated, the FE model is used to predict crack propagation at the interface and to evaluate the impact of the friction in the sensitivity analysis. According to the studies conducted above, the following conclusions can be drawn:

- The static response of the axial wrapped composite joints loaded in tension shows an linear elastic and nonlinear behaviour. The nonlinear behaviour is initiated by steel yielding as well as debonding at the composite-to-steel interface.
- The joints experienced 45% stiffness degradation during the first 100,000 load cycles under fatigue loads, after which a stabilization phenomenon is found. Only 10% stiffness is lost during the following 300,000 cycles with a diminishing trend. Cutting the specimens, after the ultimate load was achieved during the afterwards ULS test, reveals the debonding failure plane shifted from the interface to the first ply next to the interface. DIC measurements reveal that the stiffness degradation is solely due to debonding crack propagation up to 150 mm, at or near the interface, rather than a consequence of the material damage.
- Friction effects, appearing in the cracked region, are causing the crack retardation, which is concluded by the combination of 3D DIC results and FE modelling as it is shown in static and fatigue experiments. Friction coefficient at the cracked interface is measured by the tribometer and introduced in the FE model to simulate the friction effect.
- SERR values at the crack tip calculated in VCCT analysis are found to decrease from 0.85 N/mm to 0.2 N/mm when the debonding crack grows from 25 mm to 150 mm due to partial load transfer in the cracked (debonded) zone caused by the friction effect. Based on the SERR values and preliminary Paris relationship parameters, the retarded crack propagation and stabilized stiffness degradation of the joint can be predicted accurately.
- By increasing the friction effects in an FE sensitivity study through modification of the friction coefficient, a larger SERR decrease is obtained at the crack tip as the crack grows. For the sake of illustration, 30% stiffness degradation of the joint is taken as the failure criterion, 2.3 fold increase of the apparent friction coefficient (from 0.3 to 0.7) leads to 39 times longer fatigue life, where the crack growth at the debonded interface may be totally arrested and the other failure modes such as material failure may take place.

CRediT authorship contribution statement

Weikang Feng: Investigation, Data curation, Writing – original draft, Visualization. **Marko Pavlovic:** Conceptualization, Methodology, Supervision, Project administration, Funding acquisition. **Mathieu Koetsier:** Investigation, Data curation, Visualization. **Milan Veljkovic:** Supervision.

Declaration of Competing Interest

The authors declare that they have no known competing financial interests or personal relationships that could have appeared to influence the work reported in this paper.

Data availability

Data will be made available on request.

Acknowledgments

The authors would like to express their gratitude to RVO for the financial support with Topsector Energiesubsidie van het Ministerie van Economische Zaken through WrapNode-I project, and Tree Composites B.V. for the production of specimens. Acknowledgements are also made towards Pei He and Jincheng Yang for the assistance of conducting experiments and valuable discussions. The first author also would like to express his gratitude for the financial support from China Scholarship Council (CSC) under grant number of 201906260300.

Data availability

The raw/processed data required to reproduce these findings cannot be shared at this time as the data also forms part of an ongoing study.

References

[1] Pavlovic M, Bogers P, Veljkovic M. Method for making a virgin joint between two separate structural hollow sections. and Such a Virgin Joint 2021;17/052:303.
[2] He P, Pavlovic M. Feasibility of Wrapped FRP Circular Hollow Section Joints. 17th Int. Symp. Tubul. Struct., Singapore: 2020, p. 292–9. 10.3850/978-981-11-0745-0_043-cd.
[3] Feng W, Pavlovic M. Fatigue behaviour of non-welded wrapped composite joints for steel hollow sections in axial load experiments. Eng Struct 2021;249:113369. https://doi.org/10.1016/J.ENGSTRUCT.2021.113369.
[4] Feng W, He P, Pavlovic M. Combined DIC and FEA method for analysing debonding crack propagation in fatigue experiments on wrapped composite joints. Compos Struct 2022::115977. https://doi.org/10.1016/J.COMPSTRUCT.2022.115977.
[5] Khan R. Fiber bridging in composite laminates: a literature review. Compos Struct 2019:229. https://doi.org/10.1016/j.compstruct.2019.111418.
[6] Hwang W, Han KS. Interlaminar fracture behavior and fiber bridging of glass-Epoxy composite under mode I static and cyclic loadings. J Compos Mater 1989;23:396–430. https://doi.org/10.1177/002199838902300407.
[7] Yao L, Alderliesten R, Zhao M, Benedictus R. Bridging effect on mode I fatigue delamination behavior in composite laminates. Compos Part A Appl Sci Manuf 2014;63:103–9. https://doi.org/10.1016/J.COMPOSITESA.2014.04.007.
[8] Yao L, Alderliesten RC, Benedictus R. The effect of fibre bridging on the Paris relation for mode I fatigue delamination growth in composites. Compos Struct 2016;140:125–35. https://doi.org/10.1016/J.COMPSTRUCT.2015.12.027.
[9] Holmes JW, Liu L, Sørensen BF, Wahlgren S. Experimental approach for mixed-mode fatigue delamination crack growth with large-scale bridging in polymer composites. J Compos Mater 2014;48:3111–28. https://doi.org/10.1177/0021998313507613.
[10] Shivakumar K, Chen H, Abali F, Le D, Davis C. A total fatigue life model for mode I delaminated composite laminates. Int J Fatigue 2006;28:33–42. https://doi.org/10.1016/J.IJFATIGUE.2005.04.006.
[11] Chen H, Shivakumar K, Abali F. A comparison of total fatigue life models for composite laminates. Fatigue Fract Eng Mater Struct 2006;29:31–9. https://doi.org/10.1111/J.1460-2695.2006.00958.X.
[12] Liu C, Gong Y, Gong Y, Li W, Liu Z, Hu N. Mode II fatigue delamination behaviour of composite multidirectional laminates and the stress ratio effect. Eng Fract Mech 2022;264:108321. https://doi.org/10.1016/J.ENGFRACMECH.2022.108321.
[13] Yao L, Sun Y, Guo L, Zhao M, Jia L, Alderliesten RC, et al. A modified Paris relation for fatigue delamination with fibre bridging in composite laminates. Compos Struct 2017;176:556–64. https://doi.org/10.1016/J.COMPSTRUCT.2017.05.070.
[14] Tanaka K, Tanaka H. Stress-ratio effect on mode II propagation of interlaminar fatigue cracks in graphite/epoxy composites. ASTM Spec Tech Publ 1997;1285:126–42. https://doi.org/10.1520/stp19925s.
[15] Ratcliffe JG, Johnston WM. Influence of mixed mode I-mode II loading on fatigue delamination growth characteristics of a graphite epoxy tape laminate. Proc. Am. Soc. Compos. - 29th Tech. Conf. ASC 2014; 16th US-Japan Conf. Compos. Mater. ASTM-D30 Meet., 2014.

[16] Carlsson LA, Gillespie JW, Pipes RB. On the analysis and design of the end notched flexure (ENF) specimen for mode II testing. J Compos Mater 1986;20:594–604. https://doi.org/10.1177/002199838602000606.
[17] Mall S, Kochhar NK. Characterization of debond growth mechanism in adhesively bonded composites under mode II static and fatigue loadings. Eng Fract Mech 1988;31:747–58. https://doi.org/10.1016/0013-7944(88)90231-7.
[18] Gillespie JW, Carlsson LA, Pipes RB. Finite element analysis of the end notched flexure specimen for measuring mode II fracture toughness. Compos Sci Technol 1986;27:177–97. https://doi.org/10.1016/0266-3538(86)90031-X.
[19] Fan C, Ben Jar PY, Roger Cheng JJ. A unified approach to quantify the role of friction in beam-type specimens for the measurement of mode II delamination resistance of fibre-reinforced polymers. Compos Sci Technol 2007;67:989–95. https://doi.org/10.1016/j.compscitech.2006.06.011.
[20] Parrinello F, Marannano G, Borino G, Pasta A. Frictional effect in mode II delamination: experimental test and numerical simulation. Eng Fract Mech 2013; 110:258–69. https://doi.org/10.1016/J.ENGFRACMECH.2013.08.005.
[21] ISO-14129. Fibre-reinforced plastic composites - Determination of the in-plane shear stress/shear strain response, including the in-plane shear modulus and strength, by the plus or minus 45 degree tension test method. Geneva, Switzerland: ISO International Organization for Standardization; 1997.
[22] ISO/DIS-14126. Fibre-reinforced plastic composites - Determination of compressive properties in the in plane direction. Geneva, Switzerland: ISO International Organization for Standardization; 2022.
[23] ISO-527-1. Plastics - Determination of tensile properties Part 1: General principles. Geneva, Switzerland: ISO International Organization for Standardization; 2019.
[24] He P, Feng W, Pavlovic M. Influence of steel yielding and resin toughness on debonding of wrapped composite joints. Compos Struct 2023;312:116862. https://doi.org/10.1016/J.COMPSTRUCT.2023.116862.
[25] Li L, Chatzi E, Ghafoori E. Debonding model for nonlinear Fe-SMA strips bonded with nonlinear adhesives. Eng Fract Mech 2023;282:109201. https://doi.org/10.1016/j.engfracmech.2023.109201.
[26] Liu L, Wang X, Wu Z, Keller T. Tension-tension fatigue behavior of ductile adhesively-bonded FRP joints. Compos Struct 2021;268:113925. https://doi.org/10.1016/J.COMPSTRUCT.2021.113925.
[27] Olivier G, Csillag F, Tromp E, Pavlović M. Static, fatigue and creep performance of blind-bolted connectors in shear experiments on steel-FRP joints. Eng Struct 2021; 230:111713. https://doi.org/10.1016/j.engstruct.2020.111713.
[28] Wang HT, Wu G, Pang YY, Shi JW, Zakari HM. Experimental study on the bond behavior between CFRP plates and steel substrates under fatigue loading. Compos Part B Eng 2019;176:107266. https://doi.org/10.1016/j.compositesb.2019.107266.
[29] Anderson WE, McEvily AJ. Discussion: "A Critical Analysis of Crack Propagation Laws" (Paris, P., and Erdogan, F., 1963, ASME J. Basic Eng., 85, pp. 528–533. J Basic Eng 1963;85:533–533. https://doi.org/10.1115/1.3656901.
[30] Abaqus Unified FEA - SIMULIA™ by Dassault Systèmes® n.d. https://www.3ds.com/products-services/simulia/products/abaqus/ (accessed May 12, 2022).
[31] Rybicki EF, Kanninen MF. A finite element calculation of stress intensity factors by a modified crack closure integral. Eng Fract Mech 1977;9:931–8. https://doi.org/10.1016/0013-7944(77)90013-3.
[32] Mylonopoulos V. Cohesive properties of GFRP to steel bonding Cohesive properties of GFRP to steel bonding. Delft University of Technology; 2021.
[33] Yu T, Fernando D, Teng JG, Zhao XL. Experimental study on CFRP-to-steel bonded interfaces. Compos Part B Eng 2012;43:2279–89. https://doi.org/10.1016/j.compositesb.2012.01.024.
[34] Li L, Wang W, Chatzi E, Ghafoori E. Experimental investigation on debonding behavior of Fe-SMA-to-steel joints. Constr Build Mater 2023;364:129857. https://doi.org/10.1016/J.CONBUILDMAT.2022.129857.
[35] Farmand-Ashtiani E, Cugnoni J, Botsis J. Effects of large scale bridging in load controlled fatigue delamination of unidirectional carbon-epoxy specimens. Compos Sci Technol 2016;137:52–9. https://doi.org/10.1016/J.COMPSCITECH.2016.10.022.